Fusion Engineering and Design 225 (2026) 115668

Contents lists available at ScienceDirect

Fusion Engineering and Design

journal homepage: www.elsevier.com/locate/fusengdes

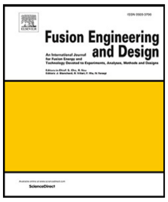

Analysis and modelling of Inner Fuel Cycle performance using exhaust bypass and Direct Internal Recycling

Federico Hattab [a,*], Yuri Igitkhanov [b], Vincenzo Narcisi [c], Alessia Santucci [c], Fabio Giannetti [a], Giulia Valeria Centomani [d], Paul A. Staniec [e], Richard Kembleton [e], Thomas Giegerich [b]

[a] Nuclear Engineering Research Group, DIAEE - Sapienza University of Rome, Corso Vittorio Emanuele II 244, 00186 Rome, Italy
[b] Karlsruhe Institute of Technology (KIT), Institute for Technical Physics (ITEP), 76344 Eggenstein-Leopoldshafen, Germany
[c] ENEA, Nuclear Department, Via E. Fermi 45, 00044, Frascati, Italy
[d] Eni S.p.A., MAFE, Venice 30175, Italy
[e] Gauss Fusion GmbH, 85748 Garching bei München, Germany

ARTICLE INFO

Keywords:
Fuel cycle
Tritium
Julia
Fusion reactors
Tritium separation

ABSTRACT

Fusion power plants require robust fuel cycle (FC) architectures that minimize tritium inventories while managing impurity build-up and isotopic imbalances. This work investigates the performance of a Inner Fuel Cycle (IFC) architecture based on the Direct Internal Recycling (DIR) concept, with an additional bypass loop for recycling of exhaust gases utilized in gas puffing. Particular focus is given to fuel dilution due to impurity accumulation and deuterium–tritium (D–T) imbalance. A new Julia-based dynamic fuel cycle modeller, MINERVA (Modelling and Integration of Nuclear fusion Energy Reactor fuel cycle for Versatile Analysis), is introduces and used to evaluate the performances of the proposed architecture and for understanding the dynamics and criticalities of a DIR-based FC. Protium build-up is identified as a potential challenge, with accumulation becoming problematic at high separation efficiencies without dedicated removal systems. Two reactor case studies are analysed, EU DEMO 2018 and Gauss Fusion's GIGA reactor. Results demonstrate that the proposed architecture effectively manages impurity concentrations below 1% for protium while maintaining optimal D–T ratios through active control systems. The proposed architecture achieves significant reductions in external fuel requirements, with effective conversion ratios growing exponentially with DIR separation efficiency. The bypass loop successfully provides the majority of gas puffing requirements without causing excessive impurity accumulation. This work establishes a foundation for advanced fuel cycle optimization studies essential for the development of commercial fusion power plants.

1. Introduction

The development of fusion power plants strongly depends on a well-designed and efficient Fuel Cycle (FC) architecture due to the innovative and challenging tasks which it shall face. The FC must supply clean fuel to the plasma while handling the processing and purification of the exhaust mixture coming from the plasma chamber and the tritium produced in the breeding blanket. These tasks shall be fulfilled while minimizing the overall tritium inventory and the losses from process inefficiencies [1].

During the operation, the consumed fuel (DT, deuterium and tritium) must be continuously replenished in the plasma chamber and the unwanted reaction products must be removed to avoid the buildup of impurities that will quench the DT reaction. To do this, a continuous matter injection system is foreseen and the plasma exhaust mixture, including both the impurities and the unburned DT fuel, is evacuated via vacuum pumping systems at the divertor region. This stream must be handled to remove impurities and recover deuterium and tritium for the reuse in the matter injection system and the processes must be as fast as possible to reduce residence time and thus inventory. One well-established approach to streamline the processes and reduce the size of the tritium-handling systems is the so-called Direct Internal Recycling (DIR) which, benefiting of the possibility to reuse deuterium–tritium mixture without full isotope separation, fulfils the function of fuel separation from impurities close to the divertor region allowing for fast reuse in the matter injection [2]. The DIR loop is part of the Inner Fuel Cycle (IFC) and is close to the Reactor Chamber (RC). It

---

* Corresponding author.
E-mail address: federico.hattab@uniroma1.it (F. Hattab).

https://doi.org/10.1016/j.fusengdes.2026.115668
Received 4 August 2025; Received in revised form 7 February 2026; Accepted 9 February 2026

is characterized by relatively short processing times (up to about one hour) and therefore limited inventories [3]. Inside the IFC there are also the Inner Tritium Plant Loop (INLT) and the Outer Tritium Plant Loop (OUTL). The remaining part of the FC is addressed as Outer Fuel Cycle (OFC) and is responsible of the extraction of tritium from the blanket side.

The DIR solution produces a pure hydrogenic stream including protium, deuterium, and tritium (hereinafter collectively referred to as Q) and an exhaust stream with the residual Q (not recovered) and impurities. The purified Q is routed back to the matter injection system enabling the fast reuse but, depending on the separation degree, it can lead to the protium buildup in the DIR loop. Such a possibility must be carefully assessed to avoid undesired fuel dilution in the plasma.

Moreover, due to the necessity of detached plasma and limited heat load and sputtering on the divertor, a considerable amount of deuterium, tritium and plasma enhancement gases (such as Ar and Ne) can be introduced in the vacuum vessel via gas puffing. This feed stream can significantly contribute to the overall throughput in the IFC and therefore, must be considered in the sizing and control of the processes [4,5].

To optimize processes and the design of the IFC, ensuring that requirements in the RC and in the recirculated fuel are met, there is the need of a fuel cycle modeller capable of simulating such phenomena. A well-established system-level fuel cycle analysis technique is that of the residence time method, computationally inexpensive and flexible [6–8]. The complexity of each subsystem is summarized in its residence time, detailing a characteristic time of processing for tritium in that component. Additionally, FC time-scales are usually not compatible with physics-based tritium transport models. Residence time models are commonly used to evaluate start-up inventory for given doubling time, and usually focus on tracking solely tritium. They lack the flexibility to implement more complex logic besides unit mass balances via differential equations.

Another approach is to use industrial process simulation software to model chemical plant equipment [3]. Such numerical platforms offer a curated and comprehensive environment for process simulations, but usually require expensive licenses and custom implementation of some components, material libraries and fluid properties (e.g. hydrogen isotopologues and isotopologues of compounds containing hydrogen such as H_2O and CH_4).

The objective of this work is to investigate the performance of a novel IFC architecture, with a focus on fuel dilution due to impurities build up and the disbalance between D and T. The subject of the work are the INTL and more internal loops, therefore the OUTL is not addressed. A new fuel cycle modeller for dynamic analysis is introduced, leveraging acasual block-based capabilities provided by the Julia ModelingToolkit language and the numerical solvers from the DifferentialEquations library [9,10]. A Julia-based framework offers several advantages over commercial process-simulation tools. Julia is purpose-built for scientific computing, enabling readable yet performant code without licence restrictions, which facilitates collaborative development and unrestricted use. Additionally, such a framework allows direct access to state-of-the-art numerical solvers, optimization libraries and more. The model presented tries to lay the base for a fuel cycle modelling platform that allows the integration of different level of complexity and control logic, building on top of the residence time method. All relevant atomic species are accounted for and a lumped 0D model of the RC allows for studies of all species considered in the IFC. Although only pseudo-transient results are presented, utilizing a dynamic model based on ODEs offers advantages by allowing more flexible system initialization and establishing a foundation for future developments that will require the dynamic capabilities.

A summary of all input data utilized for the analyses presented in this work is reported in Section 2. In Section 3, a theoretical overview of impurity constraints in a plasma is given, showing an estimation of the limit concentration of impurities in the plasma due to stability limitations. Also, protium contribution in the plasma energy balance is shown. In Section 4 the methodology used for the numerical activity is presented, showing the approach and the models. A simple DIR loop scenario is then simulated in Section 5, with the purpose of developing a deeper understanding of the dynamics of the system. In Section 6 a generalized IFC architecture is presented and applied to two reactor case studies, the EU DEMO 2018 reactor and Gauss Fusion's GIGA reactor. The design point of EU DEMO and GIGA is evaluated and the effect of key parameters is investigated.

2. Reference data

2.1. Nuclear data

Eqs. (1) to (8) are the main fusion reactions for light nuclei (branching ratios are specified for energies near the cross-section peaks) considered in this work [11].

$$D + D \xrightarrow[50\%]{} T(1.01\ \text{MeV}) + p(3.02\ \text{MeV}) \tag{1}$$

$$D + D \xrightarrow[50\%]{} \text{He}^3(0.82\ \text{MeV}) + n(2.45\ \text{MeV}) \tag{2}$$

$$D + T \longrightarrow \text{He}^4(3.5\ \text{MeV}) + n(14.1\ \text{MeV}) \tag{3}$$

$$D + \text{He}^3 \longrightarrow \text{He}^4(3.6\ \text{MeV}) + p(14.7\ \text{MeV}) \tag{4}$$

$$T + T \longrightarrow \text{He}^4 + 2n + 11.3\ \text{MeV} \tag{5}$$

$$T + \text{He}^3 \xrightarrow[51\%]{} \text{He}^4 + p + n + 12.1\ \text{MeV} \tag{6}$$

$$T + \text{He}^3 \xrightarrow[43\%]{} \text{He}^4(4.8\ \text{MeV}) + D(9.5\ \text{MeV}) \tag{7}$$

$$T + \text{He}^3 \xrightarrow[6\%]{} \text{He}^5(1.89\ \text{MeV}) + p(9.46\ \text{MeV}) \tag{8}$$

For each one, a reaction rate $\langle\sigma v\rangle$ [$\text{m}^3\ \text{s}^{-1}$], where σ [$\text{m}^2\ \text{s}^{-1}$] is the cross section and v [m s^{-1}] is the velocity, can be considered as a function of temperature obtained averaging the rates over a Maxwellian distribution [11]. The reaction rate data can be fitted to a Gamow equation as shown in Eq. (9), thus obtaining a convenient analytical formula for each reaction. The coefficients for Eq. (9) are derived via an optimization algorithm, fitting data up to 50 keV. The convergence criteria for the optimization algorithm is a Root Mean Square error lower than 1×10^{-8}. Results for each reaction are shown in Table 1, where "total" refers to the overall cross section of all reactions. Trends for the resulting fit (lines) and reference data (markers) are shown in Fig. 1 for all reactions considered. Agreement is satisfactory, and the trends highlight how at the temperatures of interest, 10–30 keV, D–D reactions have the highest rate after D–T ones. This will be important when considering protium production in Section 5.1.

$$\langle\sigma v\rangle\ [\text{m}^3\ \text{s}^{-1}] = A \times T^{-B} \times exp(-C \times T^{-D}) \times 10^{-6} \tag{9}$$

2.2. EU DEMO

For the EU DEMO tokamak, the 2018 baseline configuration is considered. Machine parameters are taken from the output of the PROCESS code, while radial temperature and density profiles come from calculations made with the ASTRA code [12,13]. Temperature T [keV] and electron density n_e [m^{-3}] profiles versus the radial coordinate along the minor radius normalized by the minor radius itself ρ [−] are reported in Fig. 2. The On-axis values are at $\rho = 0$, while $\rho = 1$ represents edge values.

Hydrogen and argon puffing values for detachment and density control are taken from plasma edge simulations made with the SOLPS-ITER code [5]. All reactor data used for preliminary calculations and fuel cycle analysis throughout the rest of this work are collected in Table 2.

Table 1
Coefficients of the Gamow equation for fusion reactions.

Parameter	$D-D(total)$	$D-T$	$D-He^3$	$T-T$	$T-He^3(total)$
A	2.794×10^{-12}	7.165×10^{-13}	3.426×10^{-14}	6.202×10^{-13}	3.530×10^{-9}
B	1.063	0.702	0.105	1.003	1.531
C	23.629	18.785	28.725	21.328	45.115
D	0.288	0.409	0.396	0.275	0.294

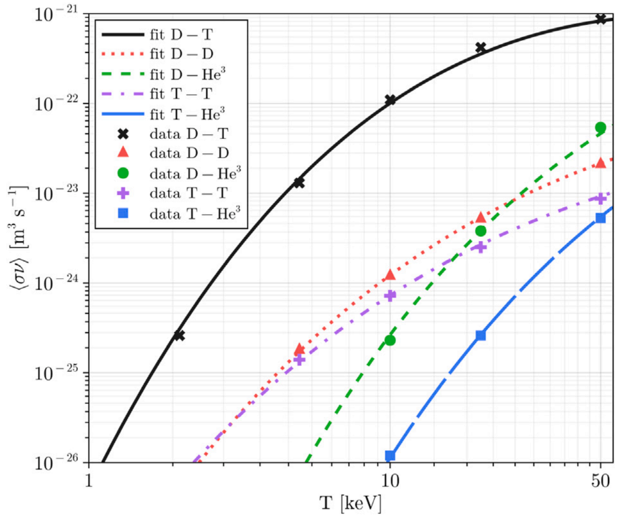

Fig. 1. Fusion reaction rates used in this work. Lines represent the fitted analytical formula, while scatter symbols are the reference data [11].

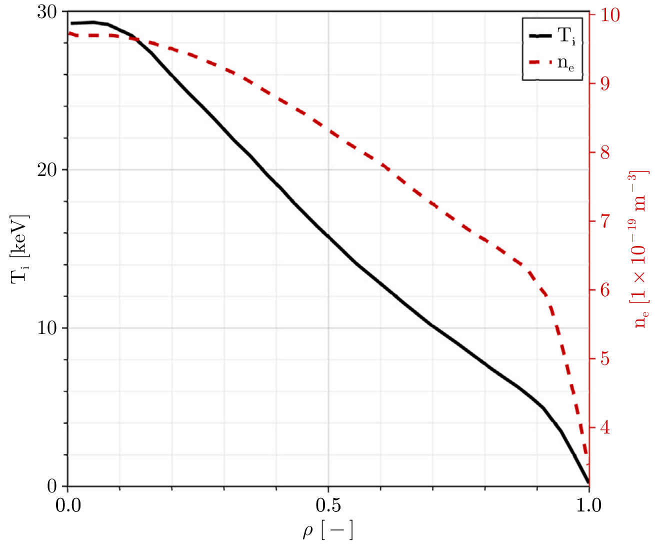

Fig. 2. Density and temperature radial profiles for the EU DEMO 2018 baseline reactor as a function of the normalized minor radius ρ.

2.3. GIGA

The numbers considered for the GIGA reactor are derived from ongoing activities and may not reflect the final design of the device. Within the scope of this work, they serve as indicative values to illustrate potential parameters of a stellarator-based power plant and allow to perform the analysis of IFC dynamics presented in Section 6. Radial density and temperature profiles along the normalized minor radius coordinate are shown in Fig. 3, while in table Table 3 the main reactor parameters used for following calculations are given.

Table 2
EU DEMO reference parameters considered.

Parameter	Value	Units	Description
R	9.073	[m]	Major radius
a	2.927	[m]	Minor radius
W_{fus}	2	[GW]	Fusion power
τ_E	3.606	[s]	Energy confinement time
τ_α^*	18.2	[s]	Effective α particle confinement time
τ_p	31.63	[s]	Particle confinement time
V_{pl}	2579	[m^3]	Plasma volume
B	5.331	[T]	Total magnetic field
β	0.02707	[−]	beta (P_{tot}^{max}/P_{mag})
S_{FW}	1462	[m^2]	First Wall surface
Γ_{Ar}^{puff}	1×10^{19}	[s^{-1}]	Ar puffing rate
Γ_{DT}^{puff}	1×10^{23}	[s^{-1}]	DT puffing rate
f_{Xe}	3.685×10^{-4}	[−]	Xe relative density in the core (n_{Xe}/n_e)

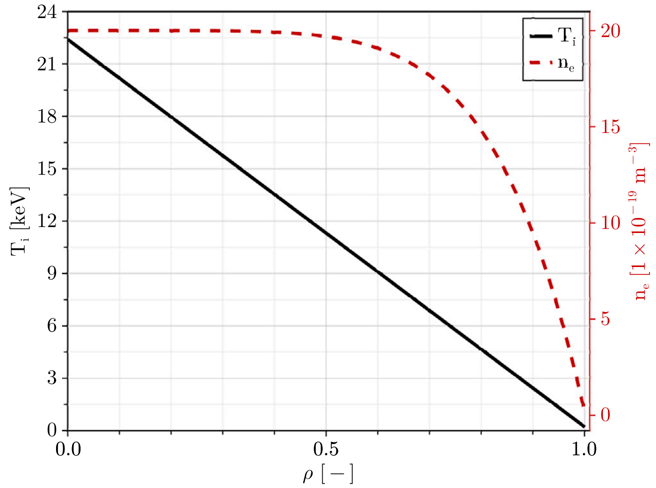

Fig. 3. Indicative density and temperature radial profiles for the GIGA reactor as a function of the normalized minor radius.

Table 3
GIGA reference parameters considered.

Parameter	Value	Units	Description
R	20.01	[m]	Average major radius
a	1.95	[m]	Average minor radius
W_{fus}	3	[GW]	Fusion power
τ_E	1.25	[s]	Energy confinement time
τ_p	6.25	[s]	Particle confinement time
V_{pl}	1500	[m^3]	Plasma volume
S_{FW}	1700	[m^2]	FW surface
$k_{S_{FW}}$	5	[−]	Effective outgassing FW surface multiplier factor
Γ_{Ne}^{puff}	1×10^{22}	[s^{-1}]	Ne puffing rate
Γ_{DT}^{puff}	1×10^{23}	[s^{-1}]	DT puffing rate

3. Physics of inner fuel cycle processes

3.1. Impurity limit due to plasma stability

A limit to the content of impurities from the point of view of plasma stability can be derived considering the factor β, representing the ratio between the total plasma pressure and the magnetic pressure [14,15]. The maximum allowable concentration of impurities ξ^{max} [−] can be defined according to Eq. (10), as the complement to one of the ratio between the fuel pressure P_{DT} and the maximum total plasma pressure P_{tot}^{max}. All pressures are given in MPa.

$$\xi^{max} = 1 - \frac{P_{DT}}{P_{tot}^{max}} \tag{10}$$

The definitions of P_{DT} and P_{tot}^{max} are given in Eqs. (11) and (12), respectively. Here n_{DT} [m^{-3}] is the average fuel density expressed as the sum of deuterium and tritium densities, T [keV] is the average temperature, B [T] is the total magnetic field, μ [H m^{-1}] is the magnetic permeability and P_{mag} is the magnetic pressure. By writing the fusion power W_{fus} (Eq. (13)) as the product of the average reaction rate $\langle\sigma v\rangle$ [m^3 s^{-1}], the square of the fuel density, the fusion energy per DT reaction E_f [MeV] and the volume of the Active Zone (AZ) V_{az} [m^3], this can be plugged in Eq. (11) to obtain Eq. (14). For a description of the AZ and how it is computed refer to Appendix A.

$$P_{DT}\ [\mathrm{MPa}] = 2n_{DT}T \times 1.6 \times 10^{-22} \tag{11}$$

$$P_{tot}^{max} = \beta P_{mag} = \beta \frac{B^2}{2\mu} 10^{-6} \tag{12}$$

$$W_{fus}\ [\mathrm{GW}] = \frac{n_{DT}^2}{4} \langle\sigma v\rangle E_f V_{az} \times 1.6 \times 10^{-22} \tag{13}$$

$$P_{DT} = \sqrt{\frac{4 \cdot 4 \cdot 1.6 \times 10^{-22}}{\langle\sigma v\rangle / T}} \sqrt{\frac{W_{fus}}{E_f V_{az}}} = K_p \sqrt{\frac{W_{fus}}{E_f V_{az}}} \tag{14}$$

By using Eqs. (12) and (14) into Eq. (10), Eq. (15) is obtained.

$$\xi^{max} = 1 - \frac{K_p}{\beta B^2} 2\mu \sqrt{\frac{W_{fus}}{E_f V_{az}}} \tag{15}$$

Considering data from Section 2, a maximum impurity concentration of 28.4% is found for EU DEMO. This is an extremely high value of impurity content and most certainly other limitations such as fuel dilution will become relevant at lower impurity concentrations (ξ values). Therefore, going forward, the limitation of impurities due to plasma stability based solely on the magnetic pressure can be neglected as it merely represents an upper bound limitation. This kind of consideration cannot be done for a stellarator since there is no global β limit, but only a localized one.

3.2. Burn curve dependence on protium

To have a more complete picture, it can be interesting to visualize the effect of protium on the burn condition of a D–T plasma. By writing a 0D plasma steady-state energy balance, so-called burn curves can be obtained [16]. The balance, as shown in Eq. (16), equates the alpha particle fusion heating to the power losses due to transport and radiation. When losses are equal to sources, the energy balance is fulfilled and the burn curve is found. Considering that the relative density of a species i is defined as $f_i = n_i/n_e$, where n_e is the electron density, f_{DT} is the relative density of the DT fuel and f_{tot} is the total relative density. R_{rad} is the radiation loss rate.

$$\frac{1}{4} n_e^2 f_{DT}^2 \langle\sigma v\rangle E_\alpha = \frac{\frac{3}{2} n_e f_{tot} T}{\tau_E} + n_e^2 R_{rad} \tag{16}$$

To plot the burn curves, Eq. (16) must be combined with the α particle balance Eq. (17), that equates the α production rate to their transport. Here τ_α^* is the α particle confinement time. After some algebra the final expression Eq. (18) is obtained, where ρ^* is the ratio between τ_α^* and the energy confinement time τ_E.

$$\frac{1}{4} n_e^2 f_{DT}^2 \langle\sigma v\rangle = \frac{n_e f_{\mathrm{He}}}{\tau_\alpha^*} \tag{17}$$

$$\frac{\frac{3}{2} T f_{tot}}{\frac{1}{4} f_{DT}^2 \langle\sigma v\rangle E_\alpha - R_{rad}} = \frac{4 f_{\mathrm{He}}}{\rho^* f_{DT}^2 \langle\sigma v\rangle} \tag{18}$$

Eq. (19)–(22) give the missing definitions used in the final balance equation. For quasi-neutrality, the electron density n_e can be written as in Eq. (19). The summation term is over all the impurity species i and is the case of coronal equilibrium, where the average impurity charge of species i $\langle Z_i \rangle$ is used, instead of summing the charge of each ionization state over all the ionization states.

$$n_e = n_H + n_D + n_T + 2n_{\mathrm{He}} + \sum_i \langle Z \rangle_i n_i \tag{19}$$

The relative density of the DT fuel can be expressed as in Eq. (20) and is also known as dilution factor, as it shows how much the plasma mixture has been diluted by helium and other impurities.

$$f_{DT} = \frac{n_D + n_T}{n_e} = 1 - 2f_{\mathrm{He}} - f_H - \sum_i \langle Z_i \rangle f_i \tag{20}$$

Using Eqs. (19) and (20) the total relative density f_{tot} is obtained (Eq. (21)).

$$f_{tot} = \frac{n_e + n_H + n_D + n_T + n_{\mathrm{He}} + \sum_i n_i}{n_e} = 2 - f_{\mathrm{He}} - \sum_i (\langle Z_i \rangle - 1) f_i \tag{21}$$

The radiation loss rate R_{rad} is defined in Eq. (22). L_i is the cooling rate for the species i and it includes the rates of bremsstrahlung, recombination and line radiation. L_i and $\langle Z_i \rangle$ are taken from [17], who derived improved polynomial fits of these quantities from nuclear data.

$$R_{rad} = (f_{DT} + f_H) L_H + f_{\mathrm{He}} L_{\mathrm{He}} + \sum_i f_i L_i \tag{22}$$

For a given ρ^* and fixed relative densities of impurities, the final energy balance Eq. (18) has only one unknown, f_{He}. For each temperature there are two possible solutions for f_{He}, meaning the plasma can burn in a low-dilution and low-radiation regime (transport limited, solid lines in Fig. 4) or in a high-dilution and high-radiation regime (radiation and dilution limited, dashed lines in Fig. 4). In [16] the analytical solution for the case of explicit radiation losses and the presence of one impurity is presented. Here, the same approach is extended numerically to an arbitrary number of impurities and is applied including Xe (as done in [18,19] for the EU DEMO reactor, where Xe is used for radiating power in the plasma core) and H. Fig. 4 shows, as a function of temperature, the triple product $n\tau_E T$ obtained by solving Eq. (18) for f_{He} and going back into Eq. (17) with the helium density found. The values of ρ^* and f_{Xe} from the EU DEMO 2018 design point have been assumed. Each curve represents the burn condition for a different protium relative density. For each curve associated with a specific value of f_H, the space outside the curve is characterized by losses greater than sources, while the space inside the curve is the possible operational space. Qualitatively, it can be seen how increasing f_H leads to a shrinkage of the curve until the energy balance cannot be satisfied anymore. For the numbers considered this happens from f_H = 7.26%.

This critical value is sensitive to the presence of other impurities and on the particle confinement time, as highlighted in Fig. 5. Values for the critical relative density of protium f_H^{crit} are shown in the presence of Xe (red dashed line) and without it (solid black line). In the presence of Xe, a heavy radiator, the allowable concentration of H drops significantly as the Xe is radiating a considerable amount of energy (although its contribution to dilution is negligible). As ρ^* increases, particles and in particular α are better confined, leading to more stringent requirements for achieving a burning plasma. This is reflected in the almost linear drop in f_H^{crit}, which basically contributes only via fuel dilution.

From this analysis we can fix a reference limiting concentration for protium at around 1%. Such value should not affect in a significant manner the operational space, should not cause an excessive drop in power due to dilution, and is compatible with the instability limit seen in Section 3.1. In the case of GIGA, confinement times are smaller than EU DEMO and no Xe seeding is expected, thus limitations on the burn

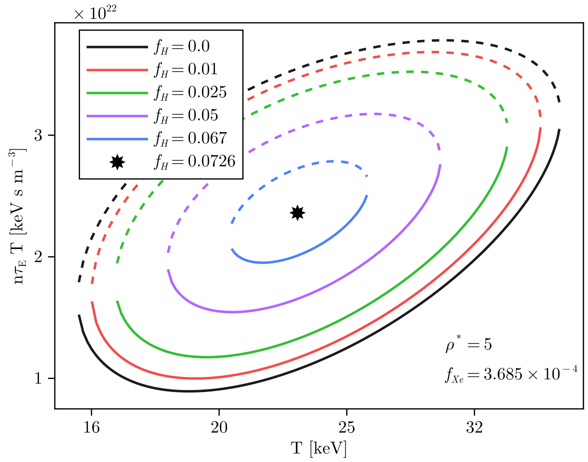

Fig. 4. Ignition parameter $n\tau_E T$ in a D–T burning plasma with addition of $f_{\mathrm{Xe}} = 3.685 \times 10^{-4}$ as a function of temperature and protium content f_H. ρ^* is fixed to 5.

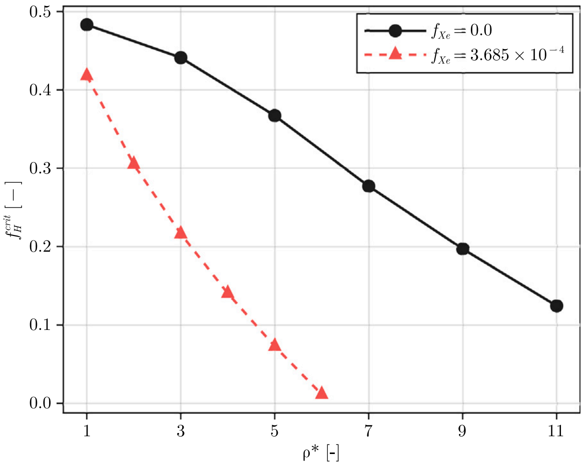

Fig. 5. Critical protium content f_H^{crit} beyond which stationary plasma burning is not possible, for different ρ^*, with ($f_{\mathrm{Xe}} = 3.685 \times 10^{-4}$) and without Xenon.

conditions should be less stringent. Since the dominant factor appears to be the drop in power due to dilution, 1% is also taken as reference, conservatively. No limits are evaluated for other impurities in the core considered in this work (i.e. Xe) as their density if fixed by the machine design ($f_{\mathrm{Xe}} = 3.685 \times 10^{-4}$ for EU DEMO and 0 for GIGA)

4. Numerical modelling approach: MINERVA

This section introduces for the first time the Modelling and Integration of Nuclear fusion Energy Reactor fuel cycle for Versatile Analysis (MINERVA) numerical model. The primary objective of the model is to estimate flows and inventories in a fusion reactor Fuel Cycle, providing full flexibility to assess various configurations. The model is developed as a collection of 0D components connected together by coupling equations. Each component is described by parameters, unknowns, ports and governing equations. An example of a generic model having one inlet and outlet flow port and a port for control is shown in Fig. 6. Parameters are values that are passed to the model to specify constant quantities. Unknowns, interchangeably called states hereinafter, are variables for which a model's equations are solved. Ports are interfaces that each block can use to exchange quantities with other blocks and are either of the flow type or signal type.

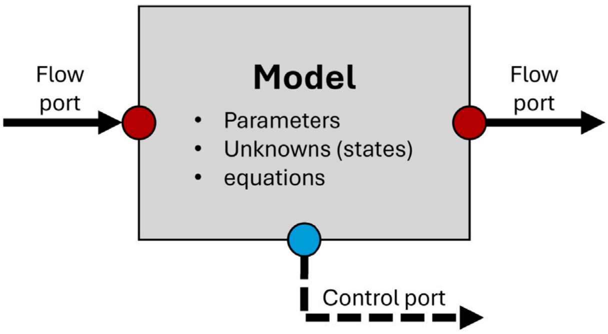

Fig. 6. Generic block model, with flow and control ports.

Flow ports are used to exchange particle flow rates and a corresponding composition. Control ports are used to exchange real values. The entire model is built with Julia ModelingToolkit and numerical solvers from the DifferentialEquations.jl library [9,10] are used for solving the Ordinary Differential Equation (ODE) system generated by ModelingToolkit.

The mathematical approach is based on the continuous-stirred tank reactor (CSTR), widely used in chemical engineering to represent a vessel into which reactions occur. The content of the reactor is assumed ideally mixed and the outlet composition is equal to that inside the reactor. Flow rate and composition at the outlet are determined by residence times and reactions rates (or more generally, sinks and sources). This approach is well established for fuel cycle analysis and is more commonly known as Residence Time Method (RTM) [7,8,20]. The mass balance for the generic model and for one species is described by the ODE Eq. (23). Here, Γ [s^{-1}] is the particle flow rate, N_i [−] is the particle inventory of species i, t [s] is time, x_i [−] is the fraction of component i, the superscripts j and k represent the inlet and outlet flows exchanged by the component. S [s^{-1}] are sinks and sources within the component, summed over all possible contributions z.

$$\frac{\partial N_i}{\partial t} = \sum_j x_i^{in,j}\Gamma^{in,j} + \sum_k x_i^{out,k}\Gamma^{out,k} \pm \sum_z S_z \tag{23}$$

Eq. (24) is the typical expression for the outlet flow rate, obtained using the residence time τ [s]. For all systems, in any point, the sum of the fractions of all species is equal to one. From here onwards, Eq. (24) is the expression used to compute outlet flow rates, unless differently specified.

$$\sum_k x_i^{out,k}\Gamma^{out,k} = x_i^{out}\Gamma^{out} = -\frac{N_i}{\tau} \tag{24}$$

Concerning the core plasma model, this represents the AZ and boundary plasma. The particles entering the plasma model are the fraction of fuel inserted into the RC that successfully penetrated the Scrape Off Layer (SOL). Inside the plasma fusion reactions are computed to determine the outlet flow, in its magnitude and composition. Species mass balances are described by Eq. (25), one for each species. V_{pl} [m^3] is the plasma volume, n_i [m^{-3}] is the species i density and RR [m^6 s^{-1}] is the integral reaction rate integrated over the AZ. w_c [−] is a correction factor for the squared density to take into account that the unknown densities are averaged over the entire plasma while reactions occur only in the AZ, and is given by the square of the ratio between the reference fuel density averaged over the AZ and the reference fuel density averaged over the entire plasma. The summation is over all reactions between species y and m that involve species i.

$$V_{pl}\frac{\partial n_i}{\partial t} = x_i^{in}\Gamma^{in} + x_i^{out}\Gamma^{out} \pm \sum_{y,m} w_c n_y n_m RR_{ym} \tag{25}$$

The integral reaction rate is computed as the integral over the active zone of the reaction rate (Eq. (26)). The densities are taken out of the integral, since they are unknowns for which we want to solve the system.

$$\Gamma_{jy} = br_{jy}ka^2 R\pi^2 \langle n^2 \rangle \int_0^{x_{AZ}} \langle \sigma v \rangle_{jy}(u) \cdot u\, du \tag{26}$$

Other models are explained as they appear in the text.

5. Study of direct internal recycling dynamics

In this section an analysis of the dynamics of the DIR loop is made using the scheme shown in Fig. 7. Although the problem is of simple analytical derivation, the solution is not straightforward without making some simplifying assumptions, due to its nonlinear nature. The full analytical treatment to derive the time evolution of protium inventory in the reactor chamber for a simple DIR configuration is reported in Appendix B. The same case has been reproduced in MINERVA and verified against the analytical solution.

Looking at Fig. 7, vacuum pumps constitute a boundary for the RC and are responsible of pumping out the unburned fuel along with any impurity present in the divertor region. The DIR Q Separation System (DSS) separates a fraction η_{DSS} of the Q in the incoming exhaust from the stream. The separated Q is sent to the buffer vessel V1, into which also some fresh fuel coming from the storage is directed. V1 is connected to the buffer vessel V2 that provides fuel to the Pellet Injection (PI) system, responsible of delivering the hydrogen mixture to the main plasma for core fuelling.

Pumps strictly obey Eq. (23) and (24), with one inlet, one outlet and a residence time. The DSS acts as a splitter for hydrogen isotopes with separation factor η_{DSS} and no inventory, since the expected processing time in candidate technologies such as metal foil pumps and permeators is negligible compared to other components. The amount $\eta_{DSS}\Gamma_Q^{in}$ is sent to V1 while the remaining throughput is sent to the outer loop. Pressure Controllers (PC) maintain pressure in vessels to a constant value by determining the aperture and closure of valves they operate on. Vessels V1 and V2 follow the generic component equations plus they are characterized by a pressure $p = \frac{R_g T}{V}(N_Q/2 + \sum_{i,i\neq Q} N_i)$ and a given setpoint pressure. These two quantities are shared with the PC for the pressure control. Except for the valve connecting V2 and PI, for which the flow rate is fixed, valves can provide a flow rate as long as there is a positive pressure difference in the direction of the flow, otherwise the flow rate is zero. The PI behaves like a standard component. The D and T storage is a generic species inventory with a pre-determined composition. The default composition is 50/50 D/T.

For what concerns RC data, this simplified case uses EU DEMO 2018 data. The values used for PI and primary vacuum pumping residence times and η_f are those described in Section 6 and reported in Table 4. For this analysis the reference η_{DSS} is assumed to be 0.8, a typical value for DIR fraction. In Section 6.1 the use of a higher value in the full IFC architecture is motivated.

5.1. Discussion

To proceed with the analysis, a few definitions should be introduced. The burning fraction, f_b, is defined as the ratio of the tritium burn from DT reactions Γ_{DT} to the rate of tritium delivered to the main plasma $\eta_f x_T^{in}\Gamma^{in}$ (Eq. (27)). Γ^{in} is the flow rate entering the RC and x_T^{in} is the atomic fraction of tritium in said flow. The parameter η_f represents the fuelling efficiency, and is defined as the ratio of the amount of matter delivered to the main plasma to the amount introduced by the matter injection system. Consequently, this definition accounts for losses resulting from ice pellet fragmentation during delivery and ablation in the SOL.

$$f_b = \frac{\Gamma_{DT}}{\eta_f x_T^{in}\Gamma^{in}} \tag{27}$$

The product $\eta_f \cdot f_b$ is known as conversion factor $\bar{f}$, and represents the ratio of tritium burn from DT reactions to the tritium fuelling rate of the machine. When dealing with a system utilizing DIR, the definition of $\bar{f}$ does not give an idea of the actual performance of the system, as the fuelling rate of the machine does not correspond to what is needed from the fuel storage. Instead, a portion (if not the majority) of the tritium delivered to the RC is made up of "recycled" fuel coming directly from the exhaust. Therefore, it is appropriate to give an alternative definition of $\bar{f}$ that highlights the effect of DIR. The effective conversion factor, f_{eff}, can be introduced, defined as the ratio of the alpha particle production rate from DT reactions to the rate of tritium incoming from the storage $x_T^{ex}\Gamma^{ex}$ (Eq. (28)).

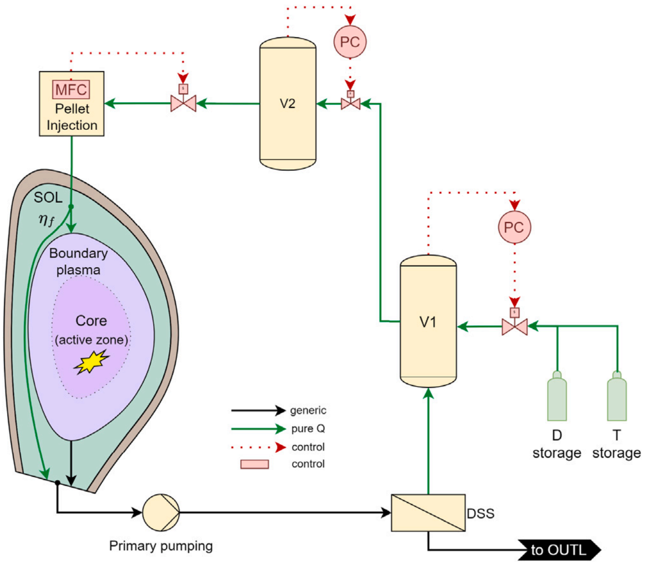

Fig. 7. Model of the DIR loop implemented using MINERVA.

$$f_{eff} = \frac{\Gamma_{DT}}{x_T^{ex}\Gamma^{ex}} \tag{28}$$

An higher f_{eff} is desirable since a higher alpha particle production rate means more efficient burn/more power, and less tritium incoming from the storage means less movement of tritium through the tritium plant (with consequent reduction of overall tritium inventory and plant size).

All simulations shown here are pseudo-transients, i.e. achieve a steady state advancing in time (the run time is one full power year). The main Figures Of Merit (FOM) used to understand trends and behaviour of the loop are f_{eff}, dilution factor (Eq. (20)) computed at the inlet of the plasma component f_d^{in}, normalized power W/W_0 and the normalized DT flow rate coming from the fuel storage $\Gamma^{ex}/\Gamma_0^{ex}$. The power is computed from n_D and n_T at the inlet of the main plasma and is normalized by the nominal value. The flow rate from the storage Γ^{ex} is normalized by the value that in absence of impurities gives the nominal reactor power.

In Fig. 8 f_{eff}, f_d^{in} and $\Gamma^{ex}/\Gamma_0^{ex}$ are shown, as a function of η_{DSS}. In accordance with what shown by [21], f_{eff} (black solid line) grows exponentially with increasing η_{DSS} because for a given fusion power we are reusing the same fuel already inside the DIR loop, requiring less fuel from the storage (green dash-dotted line). However, recirculating D and T means also recirculating H. This might lead to an unacceptable protium concentration ($\gtrsim$1% as seen in Section 3.2). As long as dilution (red dashed line) by protium due to its build-up via DIR recirculation is tolerable, the increase in η_{DSS} is beneficial as requirements on the fuel storage can be lowered. For the scenario here considered the power drop due to dilution is not appreciable up to very high ($\gtrsim$99%) separation fractions, where a sharp increase in dilution (drop of the red dashed line) is observed.

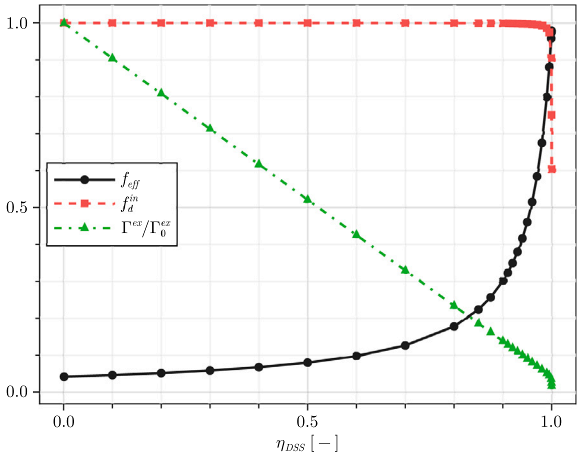

Fig. 8. Key performance metrics (effective conversion factor f_{eff}, dilution factor f_d, and flow rate from storage Γ^{ex}) of the DIR shown at steady state for different DSS separation efficiencies. The flow rate from the storage is normalized to its nominal values.

The limited build-up of H is shown in Fig. 9, where the stream composition entering (Fig. 9(a)) and leaving (Fig. 9(b)) the plasma component for different η_{DSS} are shown, respectively. The storage is supplying 50/50 DT and in the plasma reactions from Eqs. (1) to (8) occur. Among these, DT reactions (Eq. (3)) present the highest probability to occur, followed by DD reaction (Eqs. (1) and (2)), leading to a larger deuterium consumption than tritium. This is evident in Fig. 9(b) where, for $\eta_{DSS} = 0$, T content is slightly higher than D. Both are diluted, thus lower than 0.5, due to the formation of helium and protium. As η_{DSS} increases, there is the combined effect of two phenomena. On one side there is build up of H in the plasma, leading to dilution. On the other side the D/T disbalance is amplified, lowering the alpha particle production rate and, consequently, the helium production (i.e. x_{He} decreases), which is maximum for $x_D = x_T = 0.5$. Although this difference in fuel composition is small for a once-through pass in the RC, this is not the case when high recirculation takes place.

As η_{DSS} increases, there is an ever increasing but finite build up of protium. Since the H source term is small compared to the total throughput, x_H is more sensible to very high values of η_{DSS}. When η_{DSS} is such that the amount of H leaving the IFC from the DSS is less than the H source term, there is an indefinite accumulation of protium, leading to unacceptable fuel dilution. For the data considered this does happen only for very high η_{DSS}, above 0.999. The amount of protium released into the plasma chamber can exceed the formation from fusion reactions (e.g., outgassing from walls), which is the only H source considered so far, thus leading to an issue that must be assessed in the FC design phase. Moreover, although very high, it is worth noting that, depending on the technology adopted for the DSS, the separation efficiency can be even higher than the 0.999 value.

Considering now the protium outgassing rate Γ_H^{og} from metallic materials, even in the case of a tungsten First Wall (FW) it is possible that hydrogen outgassed from the structural material behind the FW may penetrate inwards through the wall. From a literature survey of outgassing from stainless steel between 150 and 400 °C, an upper bound estimate of 9.0×10^{-6} [Pa m^3 s^{-1}] per unit area is considered [22–27]. To obtain Γ_H^{og} this number is multiplied by the FW surface area. The value is quite uncertain, as it depends on temperature, geometry and other factors. If it were to be tens or a hundred times what considered here, protium build up might already be a problem for η_{DSS} lower than 0.8. This is apparent in Fig. 10, where f_d^{in} and f_{eff} are shown as a function of η_{DSS} and Γ_H^{og} (normalized by the reference value). As Γ_H^{og} increases, f_d^{in} decreases for any given η_{DSS} (the inventory of protium is increasing). The plot shown are purely for understanding the physics of the DIR as the machine clearly would not be able to operate at such high values of dilution (not considering other physical phenomena, the limits identified in Section 3 are surpassed). The effective conversion ratio promotes higher recirculation, i.e. lower Γ^{ex}, and higher alpha particle production rate, i.e. higher W. However, for high dilutions scenarios (top right corner of the f_{eff} contour), the calculation of f_{eff} becomes undefined as both the alpha particle production rate and Γ^{ex} approach zero.

Another interesting case study is the effect of a DT concentration in the storage different than 50/50. In Figs. 11 and 12 the normalized power and protium fraction at the inlet of the plasma component are shown, respectively, as a function of the fraction of tritium from the storage x_T^{ex} and η_{DSS}. The reduction of the power following a deviation from $x_T^{ex} = 0.5$ is stronger the more η_{DSS} increases, as the amplifying effect of the DIR on the fuel disbalance becomes more significant. For protium a significant build up is observed in the case of detuerium-prevalent mixtures, since the main source term of H in the plasma are D–D reactions. Actually, due to the combined effect of protium accumulation and fuel disbalance, the optimum from the point of view of power production is not for $x_T^{ex} = 0.5$ but for slightly higher values of x_T^{ex}. This can be seen by considering two slices on the (x_T^{ex}, W/W_0) plane in Fig. 11, one at $\eta_{DSS} = 0.001$ and one at $\eta_{DSS} = 0.999$, and a slice on the (x_T^{ex}, x_H^{in}) plane in Fig. 12 at $\eta_{DSS} = 0.999$. For no recirculation there is no appreciable fuel dilution and no amplification of the fuel disbalance due to DIR. Thus, the maximum power lies exactly at $x_T^{ex} = 0.5$. For high recirculations the maximum is still close to the 0.5 value but is shifted to the tritium-dominant side ($x_T^{ex} = 50.3\%$) due to the protium build up, which is considerably more pronounced on the deuterium-dominant side the plot. It must be noted that if also outgassing is counted and depending on its intensity the deviation from $x_T = 0.5$ would happen at lower η_{DSS}.

The results provided in this section highlight the dynamics of the DIR loop and show that, with such architecture, the fuel rebalancing and the protium removal are functions required inside the FC. The mixture coming from the storage towards the fuel system should be actively monitored and adjusted, especially for scenarios where most Q is re-used via DIR, to guarantee that the fuelling system can deliver a 50/50 DT mixture. Starting from the outcomes of this analysis, a more complex IFC is studied in the next section.

6. Inner fuel cycle architecture

The architecture for a generalized IFC is introduced in Fig. 13. Compared to what presented in Section 5, architectural changes and key components have been introduced. The architecture considered is organized in three areas (loops). The green area, i.e. the DIR loop, has not changed conceptually compared to Fig. 7. The DSS separates a fraction η_{DSS} of the Q in the incoming flow and sends it to the vessel V1. V1 then feeds the vessel V2, which is responsible of delivering fuel to the pellet injection system. One notable difference is the possibility to add a plasma enhancing gas, Xe, in the inlet of the PI system for core radiative seeding. The control system of V1 is also different compared to what presented in Section 5. It ensures that the D/T ratio in the buffer vessel V1 is kept at 50/50, addressing the need for isotope rebalancing. For the management of protium inventory, a splitter S2 separates a portion η_{S2} of the Q coming from the DSS and sends it to the blue loop, the INTL, where the Protium Removal (PR) produces a protium-depleted stream, sent to V1, and a protium-enriched stream, exchanged with the OUTL. The major architectural change is the presence of the bypass loop (grey area). A splitter S1 separates the fraction η_{S1} of the machine exhaust as it is, and sends it to the buffer vessel V3. The purpose of the bypass is to supply a portion of the gas puffing rate required for density control without performing any separation process on the mixture handled. V3 is pressure controlled, like other vessels, and in the case the flow coming from S1 is not sufficient to keep its operational pressure, fuel is taken from V1. V1,

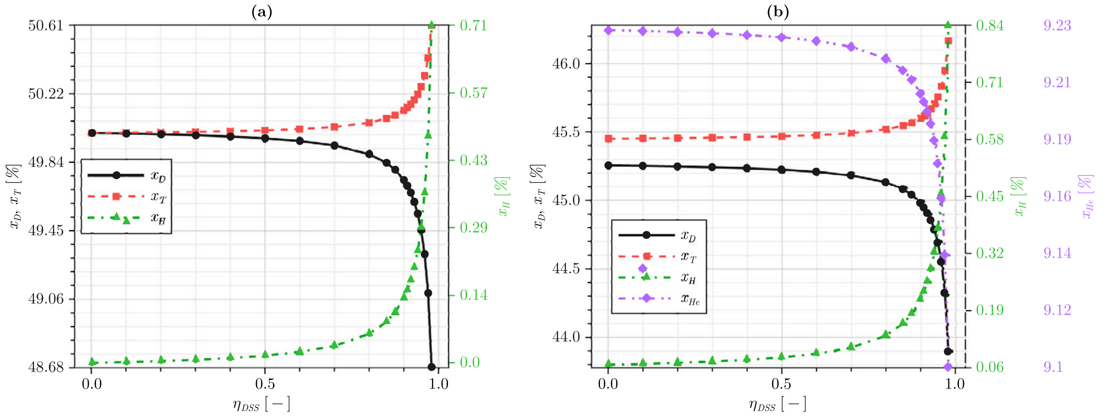

Fig. 9. Composition at the inlet (a) and outlet (b) of the plasma model at steady state for different DSS separation efficiencies.

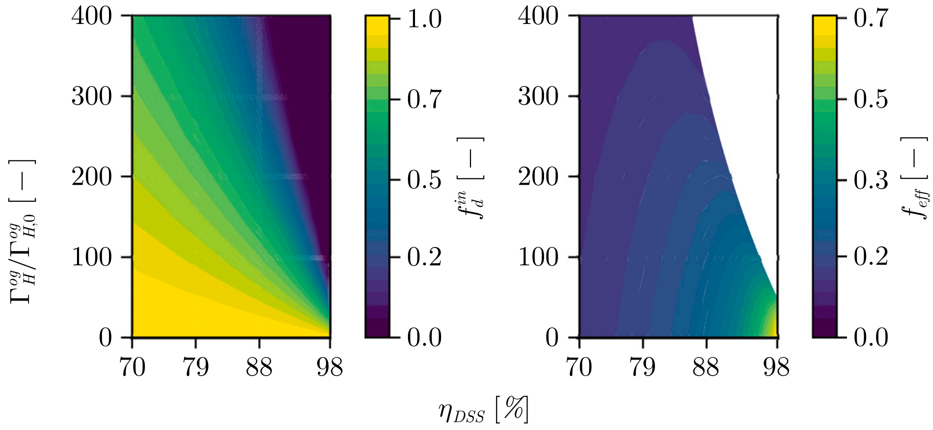

Fig. 10. Dilution factor f_d^{in} (left) and effective conversion factor f_{eff} (right) as a function of H outgassing and DSS separation efficiency.

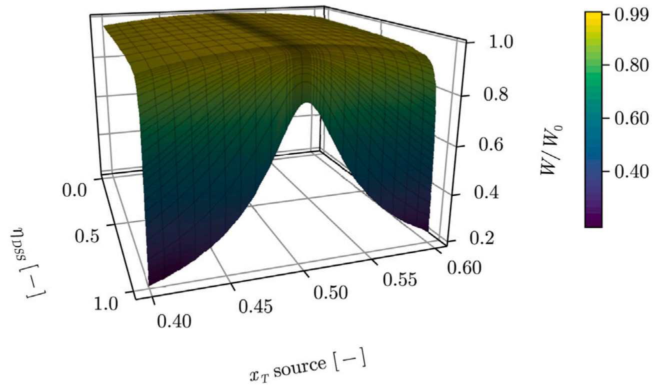

Fig. 11. Normalized power as a function of tritium fraction x_T from the external source and DSS separation efficiency η_{DSS}.

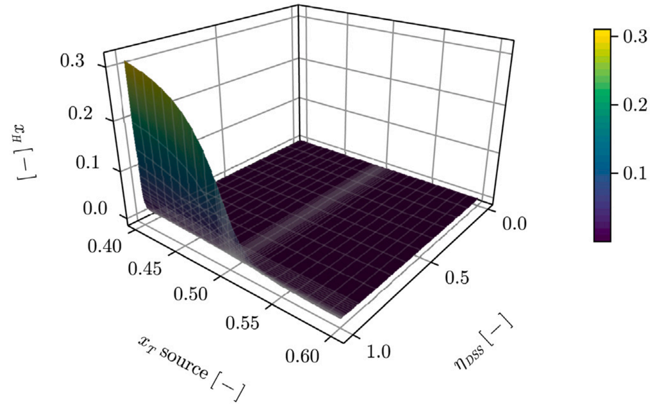

Fig. 12. Protium fraction x_H at the inlet of the plasma model as a function of tritium fraction x_T from the external source and DD separation efficiency η_{DSS}.

together with the control on the storage, acts as a gas distribution and control system. There is no active control on the amount of noble gas used for detachment control being recycled via the bypass loop and the required amount is taken from the storage, as it needs to be delivered to that specific location.

It is important to note that the DT puff rate may be several times greater than the amount of pellet injection used for core fuelling. Therefore, from a FC perspective, density control puffing is assumed to involve both D and T rather than solely D, as the latter scenario would significantly dilute the overall fuel within the system and increase loads to the fuel cycle. The use of recycled exhaust gases for detachment control puffing purposes is under investigation. If the accumulation of impurities remains within acceptable limits, this approach could reduce the overall size and inventory of the fuel cycle by providing a rapid and cost-effective source of puffing gas and lowering requirements on the downstream tritium plant. Since this work focuses on the system-level dynamics, it is yet to be seen what are the limitations within the RC to the recirculation of impurities, as this might represent a limit to the fraction of throughput that can be sent from S1 to the buffer vessel V3.

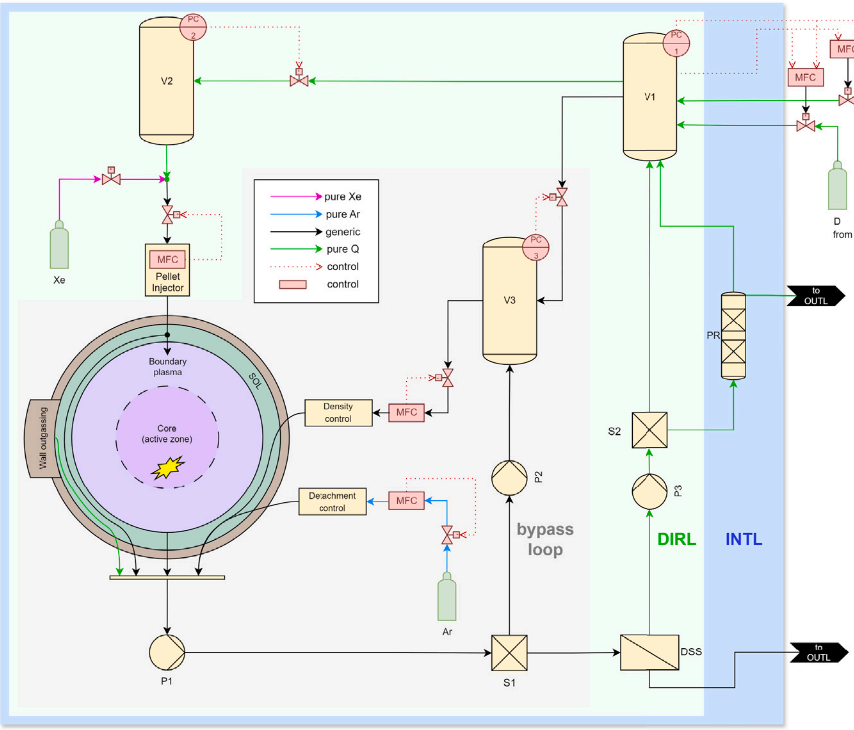

Fig. 13. IFC architecture considered.

6.1. IFC modelling

The architecture in Fig. 13 has been implemented in MINERVA according to the methodology presented in Section 4. The storage control system, that ensure the D/T ratio in V1 remains at 50/50, consists of two separate PIDs controlling the D and T partial pressures and thus particles number in V1. Each PID (one for D and one for T) measures the current particle number, compares it with the reference value and acts on the storage valve.

A set of reasonable parameters for the IFC architecture is provided and summarized in Table 4. The fuel puff rate, combined with the Ar puff rate in the divertor region needed for detachment control, is uncertain and a wide range of values can be found from literature [4]. Regarding the EU DEMO 2018, a potential operational scenario has been investigate by [5], which provides estimates for fuel and Ar puffing rates. The results from this study are utilized as reference. S1 is a limited splitter, meaning that it is characterized by a maximum amount of gas it can recirculate, in this case that value is the total fuel puff rate.

Now that also the INTL is being considered, there should be an Exhaust Processing System (EPS) that guarantees the recycling of as much Q as possible in the INTL and the innermost loops to limit the tritium load to the OUTL. According to the architecture presented this function is assigned to the DSS itself. This, combined with the presence of the PR system, motivates an higher η_{DSS} with respect to what considered in Section 5. An η_{DSS} of 99.5% is assumed as reference value going forward and a sensitivity across its entire possible range is done. A similar methodology is applied to the bypass split fraction η_{S1}. The chosen η_{S1} values differ between the two reactors examined, due to the different reactor design, thus required throughput for core fuelling, and different gas puffing requirement. The criterion is to supply the majority of the gas required for density control via the bypass loop. Also for η_{S1} a parameter scan over the full range is conducted.

The PR unit works according to Eqs. (23) and (24), with the difference that the outgoing flow rate is distributed between its two outlets according to isotope-specific separation fractions. The parameters for the PR unit are based on estimations derived from the HESTIA facility, which utilizes a Temperature Swing Adsorption (TSA) process [28]. Due to the operational principles of this system, for a given protium removal efficiency η_{PR}, the corresponding separation fractions for D and T are taken as $\frac{\eta_{PR}}{\sqrt{2}}$ and $\frac{\eta_{PR}}{2}$, respectively. This component represents the slowest piece of the IFC, and it is desirable to minimize the fraction of purified exhaust η_{S2} that is directed to it.

Table 4
IFC reference parameters.

Parameter	Value DEMO/GIGA	Units	Description
η_{DSS}	0.995	[–]	DSS Q separation efficiency
η_{S1}	0.75/0.32	[–]	Splitter S1 splitting fraction
η_{S2}	0.2	[–]	Splitter S2 splitting fraction
η_f	0.25	[–]	Fuelling efficiency
η_{PR}	0.83	[–]	H PR separation efficiency
τ_{PR}	2400	[s]	PR residence time
τ_{PI}	1200	[s]	PI residence time
τ_{P1}	120	[s]	Vacuum pumping P1 residence time
τ_{GP}	30	[s]	Gas puffing residence time
V_{V1}, V_{V2}, V_{V3}	0.1	[m^3]	Vessels volumes
p_{V1}, p_{V3}	0.8	[bar]	Vessel V1, V3 operating pressure
p_{V2}	0.9	[bar]	Vessel V2 operating pressure
T_{V1}, T_{V2}, T_{V3}	300.15	[K]	Vessels operating temperature
Γ_H^{og}	9×10^{-6}	[Pa m s^{-1}]	Wall H outgassing rate per unit surface

The reference η_f for EU DEMO is obtained from extrapolations of DIII-D studies [29]. The same number is momentarily assumed also for GIGA until better estimations are available. For what concerns pellet injection, a residence time of the order of a few tens of minutes is expected [7,30]. For the divertor pumping of the EU DEMO reactor a processing time of 120 s is estimated from modelling results of the “KALPUREX” process [31].

The FC simulations of the two reactors are test cases to study the architecture presented. The same FC values used for EU DEMO in Table 4 are considered also for GIGA, except for S1 separation fraction due to the different machines throughput.

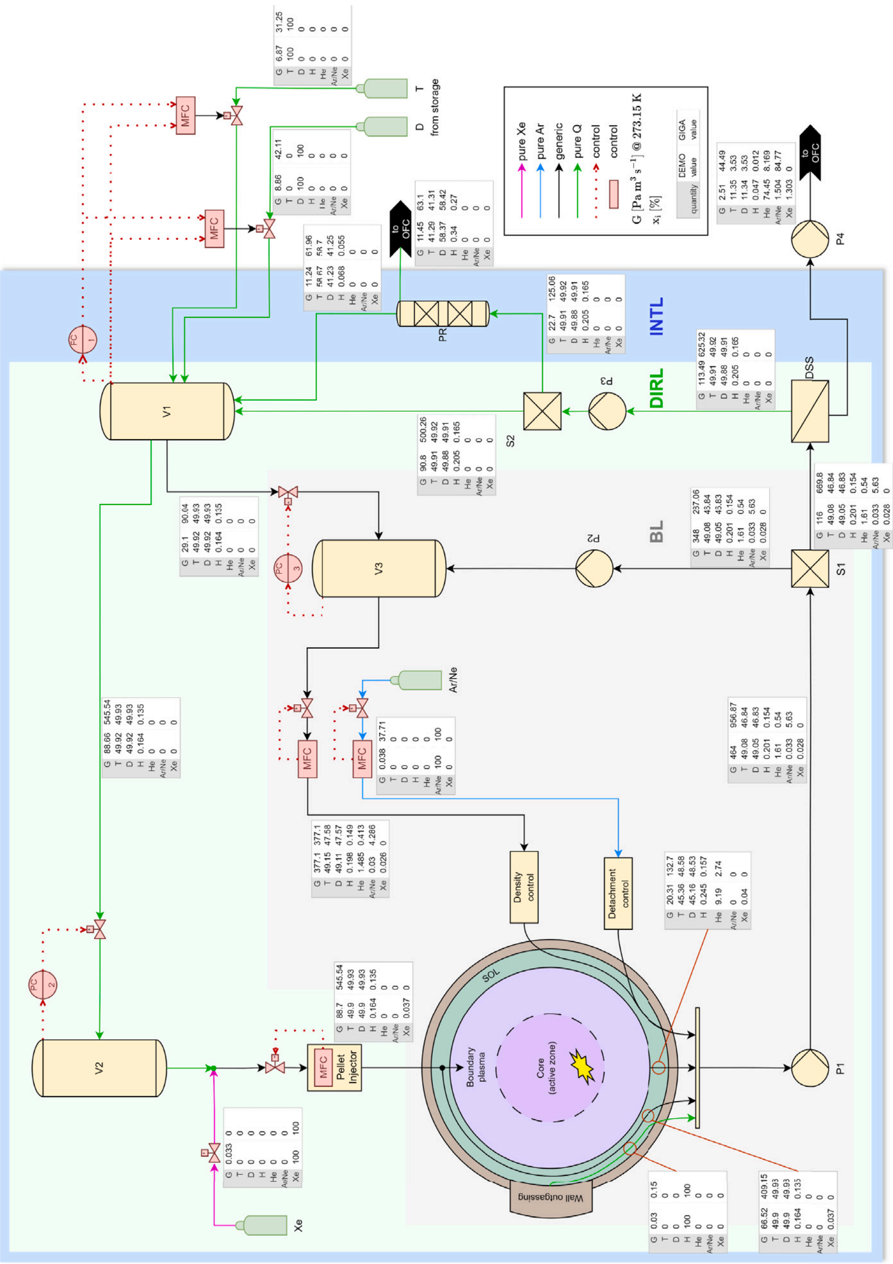

Fig. 14. IFC architecture considered and steady state results (throughput G [Pa m^3 s^{-1}] and atomic compositions x_i [%]) for EU DEMO and GIGA.

6.2. Discussion

6.2.1. EU DEMO

Steady state flows and compositions for the reference case are shown in Fig. 14 (first numeric column of boxes). All impurities reach a stable value, with H staying well below the 1% assumed as limit concentration. The bypass loop does not cause significant accumulation of impurities, since the fraction of machine throughput leaving the bypass loop (1-η_{S1}) is a sufficient sink of He, Ar and Xe. For the reference η_{DSS} value of 99.5%, protium removal is mandatory, as its absence would lead to a H fraction in the pellets of 6.5%. To ensure that fuel pellets are made of 50/50 D/T, the ratio of D over T required from the storage is about 1.29. This difference is largely due to the strong isotopic effect of the PR system.

In Fig. 15 steady state figures of merit (Fig. 15(a)) and Q and He atomic fractions at the exhaust (Fig. 15(b)) for different η_{DSS} are shown. The overall trends align with those discussed in Section 5.1 with some notable differences. The trends of the normalized fuel flow rate from the source Γ^{ex} and of the dilution factor f_d^{in} do not show the sharp decline for $\eta_{DSS} \rightarrow 1$ because the PR avoids uncontrolled H buildup, with f_d^{in} remaining almost constant. However, the fuel removed by the PR needs to be taken from the storage, causing f_{eff} to grow less compared to the DIR case. This stability is attributed to protium removal and fuel composition control, which also influence the trends observed in Fig. 15(b), resulting in an almost unchanged x_{He}. The use of PR at very high DIR fractions effectively limits H accumulation, maintaining it below 0.22%. The fractions x_{Xe} and x_{Ar}, not shown in Fig. 15(b), stay constant at 0.028% and 0.033%, respectively. Γ^{ex} here is normalized relative to the amount of fuel that would need to be taken from the storage if recirculations were not employed. Consequently, the denominator accounts for both the fuel puff rate and the throughput sent to the PI system. Even when η_{DSS} is zero, the presence of the bypass loop causes a significant portion of the total throughput to go back into the RC via S1, resulting in a low maximum value for $\Gamma^{ex}/\Gamma_0^{ex}$.

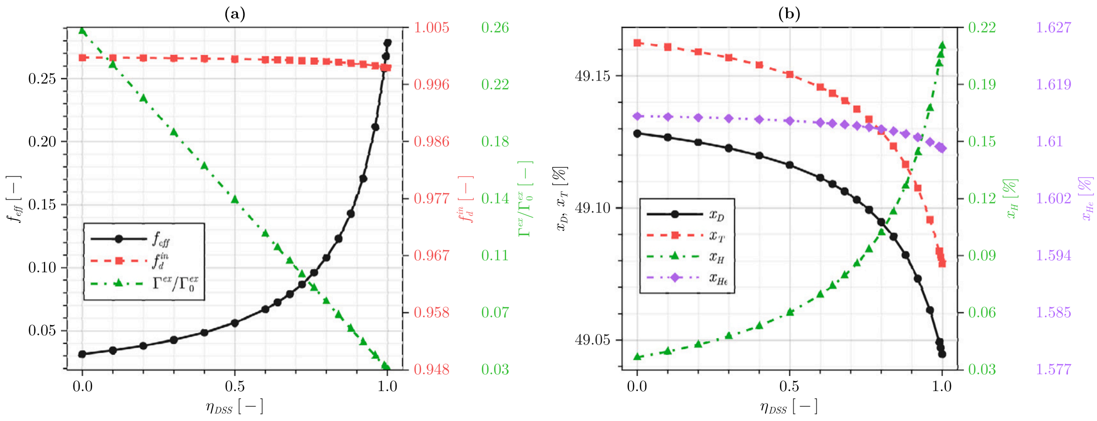

Fig. 15. EU DEMO IFC figures of merits (plot (a), f_{eff}, f_d^{in}, $\Gamma^{ex}/\Gamma_0^{ex}$) and hydrogen and helium composition at the primary vacuum pumping location (b) for different DIR separation fractions η_{DSS}.

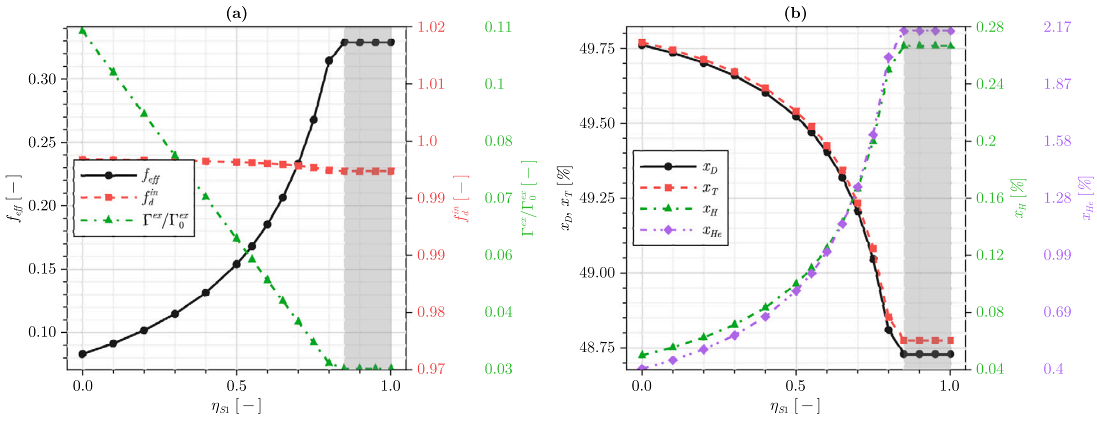

Fig. 16. EU DEMO IFC figures of merits (plot (a), f_{eff}, f_d^{in}, $\Gamma^{ex}/\Gamma_0^{ex}$) and hydrogen and helium composition at the primary vacuum pumping location (b) for different bypass loop split factors η_{S1}.

Nonetheless, higher DIR separation help reducing loads to processes downstream the IFC, which is required since they are the ones with the highest tritium processing times.

Fig. 16 presents steady-state figures of merit (Fig. 16(a)) and the atomic fractions of Q and He at the exhaust (Fig. 16(b)) for the entire range of possible η_{S1}. It is observed that the splitter S1 operates at its maximum capacity around $\eta_{S1} = 0.85$, at which point it directs the maximum allowable flow to V3, corresponding to Γ_{DT}^{puff}. Increasing η_{S1} beyond this point (grey area in Fig. 16) does not result in further changes to the flow rate reaching V3. This cut-off is clearly visible in the green dash-dotted line in Fig. 16(a) and its effect is also reflected on f_{eff}, stabilizing on an almost constant value since dilution remains unaffected by the bypass loop, with f_d^{in} equal to one across the entire range. Compared to Fig. 15 an improvement in f_{eff} can be seen increasing η_{S1}. On the other hand, at the reactor exhaust (Fig. 16(b)) there is a noticeable accumulation of H and He, although their fractions, up to 0.28% and 2.17% respectively, remain within expected acceptable limits. Both Xe and Ar fractions at the pumping location remain below 0.045%.

6.2.2. GIGA

Steady state flows and compositions for the reference case are displayed in Fig. 13 (second numeric column of boxes). All quantities attain stable values, with H remaining well below the 1% mark. Due to the relatively high Ne puffing rate, a Ne concentration of 5.63% is reached in the exhaust.

Based on the scenario considered, GIGA's total throughput is higher than that of EU DEMO. This is primarily due to shorter confinement times, higher power, and a supposed higher puff rate of radiating gas. Consequently, the burn rate is reduced, resulting in overall lower He concentrations. Additionally, the puff rate considered is closer to the pellet injection rate, leading to a smaller fraction of the throughput sent to V3 and thus a relatively small build up of impurities via the bypass loop compared to the absence of bypass. Although the outgassing rate is considerably higher than in EU DEMO due to the increased effective surface area, a small concentration of protium, 0.154%, is established once all streams are combined at the exhaust. The ratio of D over T required from the storage is 1.35, mainly due to the PR system.

In Fig. 17 steady state figures of merit (Fig. 17(a)) and Q and He atomic fractions at the machine exhaust (Fig. 17(b)) for different η_{DSS} are shown. Looking at Fig. 17(a), trends are the same as in EU DEMO, but quantitatively different. In GIGA the amount of gas throughput sent from S1 to V3 (bypass loop) is around 30% the total exhaust, thus increasing η_{DSS} strongly affects $\Gamma^{ex}/\Gamma_0^{ex}$, going from 0.7 at $\eta_{DSS} = 0$ to 0.08 at $\eta_{DSS} = 1.0$. The consequent increase in the flow rate through the DIR leads to an f_{eff} that is half that of EU DEMO. The f_{eff} is, for GIGA, relatively small even at very high η_{DSS} due to the short confinement times and thus the burn rate. The PR system ensures that f_d^{in} is around unity also when all the exhaust Q passing through the DSS is routed through the DIR. The same result is observed in EU DEMO, meaning that the PR effect is independent on the flow rates that it elaborates (which will instead determine the sizing of the component). Trends in Fig. 17(b) are the same as those in Fig. 15(b), with the key difference that D and T fractions are a bit lower than the case of EU-DEMO because there is a constant fraction of Ne equal to 5.63%. Compared to EU DEMO protium concentrations are similar, while helium buildup is significantly smaller, sitting at about 0.54% at the exhaust.

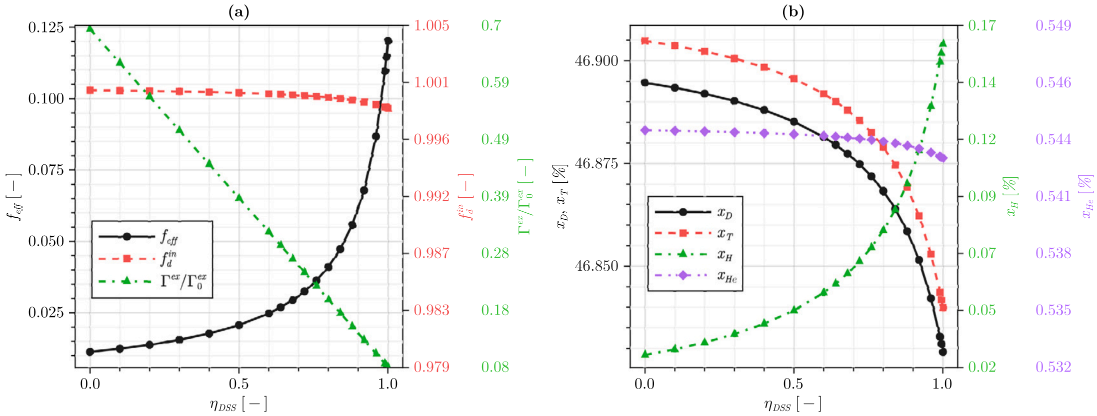

Fig. 17. GIGA IFC figures of merits (plot (a), f_{eff}, f_d^{in}, $\Gamma^{ex}/\Gamma_0^{ex}$) and hydrogen and helium composition at the primary vacuum pumping location (b) for different DIR separation fractions η_{DSS}.

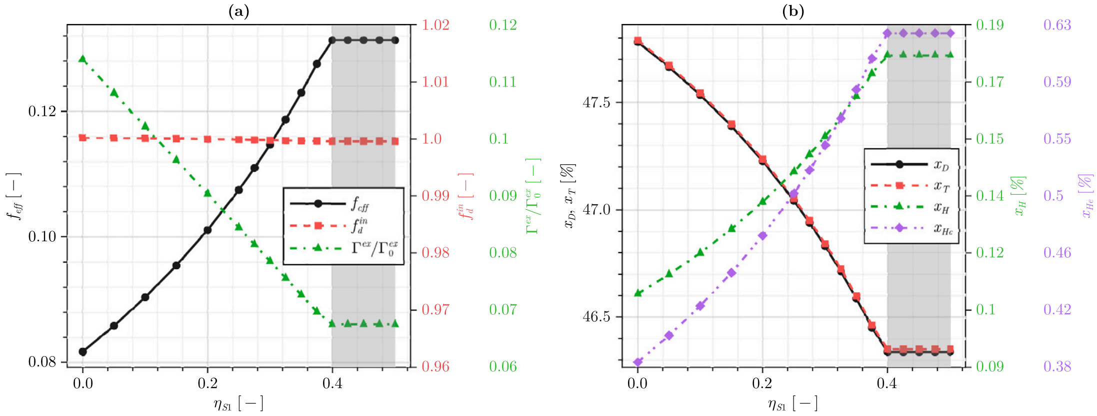

Fig. 18. GIGA IFC figures of merits (plot (a), f_{eff}, f_d^{in}, $\Gamma^{ex}/\Gamma_0^{ex}$) and hydrogen and helium composition at the primary vacuum pumping location (b) for different bypass loop split factors η_{S1}.

Fig. 18 is the analogous of Fig. 16, and the trends are the same. In this case the Ne fraction goes from 3.94% to 6.5% and S1 full capacity is reached around $\eta_{S1} = 0.4$, limiting the possible reduction of Γ^{ex}. Given the exponential dependence of f_{eff} on η_{S1}, its possible increase is limited because the majority of the benefit comes at high split values. The effect of the bypass loop on f_d^{in} is negligible, while He and H content at the exhaust exhibit an almost doubling in value when going from no bypass to $\eta_{S1} = 0.4$, but they are still low in absolute value, reaching a maximum of 0.65% and 0.18%, respectively.

6.2.3. *Sensitivity analysis*

According to what shown in Sections 6.2.1 and 6.2.2, the fundamental behaviour of the IFC remains consistent across different machine configurations under the conditions examined. Given the preliminary set of parameters considered and modelling assumptions made, due to shorter confinement times and a higher assumed noble gas puffing rate, the resulting total throughput of GIGA is larger than that of EU DEMO. At the interface with the OUTL, the flow rate in EU DEMO exhibits a higher tritium fraction, which suggests that the effort required for tritium separation in the DSS and downstream systems will be lower. Overall, impurity levels within both the bypass and DIR loops are higher in the GIGA scenario. It is to be assessed how the composition of the puffed mixture affects detailed dynamics inside the reactor chamber. These differences affect the composition of what is sent outside of the IFC for further processing. In EU DEMO, the exhaust mixture going out of the IFC from the DSS predominantly consists of He, whereas this is not the case in GIGA mainly due to the assumed Ne puff rate. Another interesting point is that changing machine and operating conditions, the architecture manages to guarantee a similar (and limited) disbalance between D and T isotopes. Such disbalance is mainly attributed to the working principle of the PR.

This section aims to evaluate the relative importance of key parameters with respect to the effective conversion rate f_{eff} and the dilution factor at the pellet fuelling location f_d^{in}. f_{eff} is chosen as it depends on both dilution and quality of fuel recirculation, therefore it is a comprehensive metric for the whole IFC. f_d^{in} is another parameter that requires careful monitoring when recirculating fuel back into the main plasma, and its dependence on selected quantities also helps better understanding the trends of f_{eff}, as more dilution means less power and a smaller numerator of f_{eff}. Since the behaviour of the architecture is consistent across the configurations examined, the analysis presented here is focused solely on EU DEMO, providing a qualitative assessment. The sensitivity analysis conducted is of the One-At-a-Time (OAT) type, wherein each parameter is varied individually while holding all other parameters at their baseline values. This method allows for the evaluation of each parameter's impact on the model outputs. Eight parameters have been selected for this study: τ_p, η_f, Γ_{DT}^{puff}, Γ_H^{og}, η_{DSS}, η_{PR}, η_{S1}, η_{S2}. The ranges of variation for these parameters and their baseline values are detailed in Table 5. Each range is divided in 10 intervals, is centred around the value μ, and goes from $\mu - \delta$ to $\mu + \delta$.

To compare the sensitivity across parameters with different scales and units the relative sensitivity index coefficient RS can be introduced according to Eq. (29) to represent the percentage change in output per percentage change in input.

$$RS_i = \frac{\partial y}{\partial x_i} \cdot \frac{x_i}{y} \approx \frac{\Delta y / y}{\Delta x_i / x_i} \tag{29}$$

Table 5
IFC OAT sensitivity analysis parameters and ranges.

Parameter	Mean μ	Units	Range $\pm\delta$ [%]	Description
τ_p	31.63	[s]	±50	Particle confinement time
η_f	0.25	[–]	±60	Fuelling efficiency
Γ_{DT}^{puff}	1×10^{23}	[s^{-1}]	±60	Fuel puff rate
Γ_H^{og}	9.0×10^{-6}	[Pa m^3 s^{-1}]	±100	Wall H outgassing rate
η_{DSS}	0.995	[–]	±0.5	DIR Q separation efficiency
η_{PR}	0.835	[–]	±20	PR H separation efficiency
η_{S1}	0.75	[–]	±33	Splitter S1 split factor
η_{S2}	0.2	[–]	±50	Splitter S2 split factor

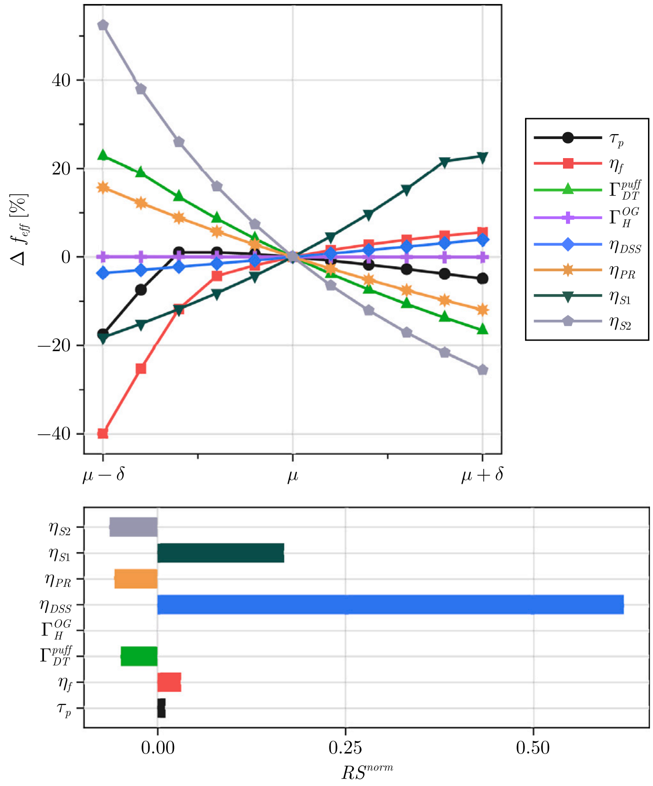

Fig. 19. EU DEMO global sensitivity analysis, f_{eff}.

where Δy is the change in output due to a change in Δx_i and y is the output at the reference value x_i. For any given parameter i, if RS_i is divided by the sum of all relative sensitivity indices, the normalized relative sensitivity index RS_i^{norm} is obtained (Eq. (30)). RS_i^{norm} can be interpreted as a weight of the parameter i in influencing the output and is useful for the ranking of parameters.

$$RS_i^{norm} = \frac{RS_i}{\sum_j |RS_j|} \tag{30}$$

Fig. 19 presents sensitivity analysis results for the effective conversion factor f_{eff}. The top plot illustrates the percentage variation of the output with respect of the reference state across the input parameter range $[\mu-\delta,\ \mu+\delta]$, for each parameter considered. The bottom plot displays the normalized relative sensitivity index coefficient.

The dominant factors influencing f_{eff} are the fractions of exhaust recycled by DIR (η_{DSS}) and bypass loops (η_{S1}). These determine the fuel requirement from storage by effectively setting the value of the denominator in the definition of f_{eff}. Higher recycling fractions reduce the need for fresh fuel, thus increasing f_{eff}. A reduction in the fuel puffing rate increases f_{eff} due to reduced total throughput. Sending gas to the PR unit (η_{S2}) or improving its efficiency (η_{PR}) aids in fuel cleanup, however, the beneficial effect of protium removal is overshadowed by the associated loss of fuel from the H-enriched stream leaving the IFC. Low fuelling efficiencies lead to a sharp increase in throughput with a $1/\eta_f$ trend. Lastly, varying particle confinement time from $\mu-\delta$ to $\mu+\delta$ causes a decreasing trend for both the alpha particle production rate and Γ^{ex}, however the slope of the latter for shorter times is much steeper, resulting in the trend for τ_p shown in Fig. 19. Although the variation in f_{eff} due to η_{DSS} looks small, the normalized relative sensitivity index gives it the most importance because of the small variation range $\delta = \pm 0.5\%$. For lower values of η_{DSS}, below 99%, the relative importance of the parameter decreases.

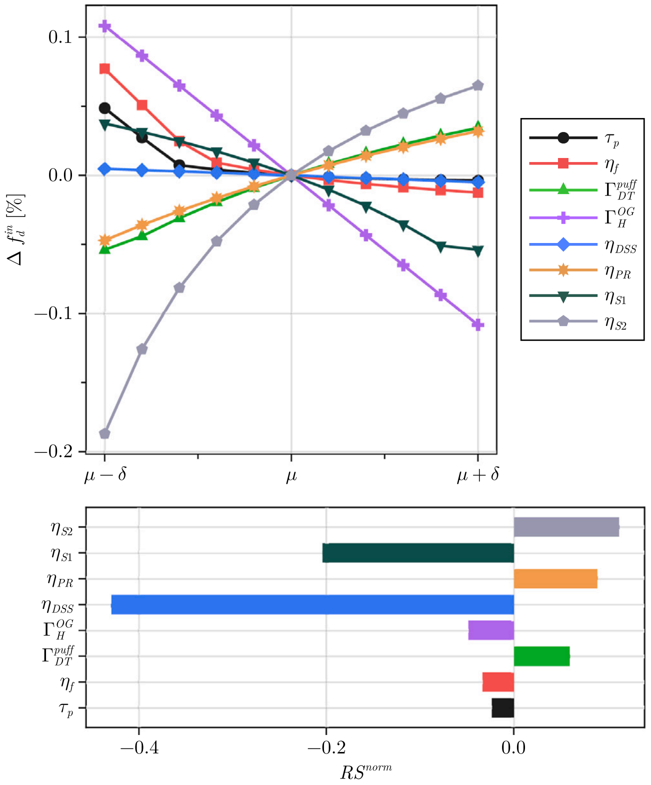

Fig. 20. EU DEMO global sensitivity analysis, f_d^{in}.

Fig. 20 shows the sensitivity analysis for f_d^{in}. There are clear analogies with Fig. 19, as most curves have the same trend but with inverted sign. One notable difference is that now the effect of protium wall outgassing Γ_H^{OG} is noticeable and linearly proportional to its value. The larger the H source term the smaller f_d^{in} becomes, meaning that accumulation of H grows. Increasing the split fractions of the bypass loop causes an increase of H concentration at the exhaust and a reduction in fresh fuel from the storage (as seen in Figs. 16 and 18), leading to a smaller f_d^{in}. The same net effect is observed for the DIR split fraction.

When less fuel is purified from H, either by using the splitter S2 or by decreasing the efficiency of the PR system, protium accumulates more and f_d^{in} decreases. If the rate of H removal approaches the rate of H production, dilution increases sharply as shown for smaller values of η_{S2}.

7. Conclusions

In this work a comprehensive investigation of Inner Fuel Cycle dynamics for fusion reactors, introducing both theoretical frameworks and practical modelling tools for fuel cycle analysis is presented.

Concerning tokamaks, the analysis of impurity limits reveals that plasma stability constraints based on magnetic pressure alone are relatively permissive, with dilution effects becoming the dominant limiting factor. Protium concentrations up to approximately 1% have minimal impact on burn curves, but beyond critical thresholds (around 7.26% for the EU DEMO conditions studied), the plasma energy balance cannot be maintained. The presence of heavy impurities like xenon significantly reduces allowable protium concentrations due to enhanced radiative losses.

An analytical solution for the protium inventory evolution in time in the plasma is derived, accounting for only D–T reactions or for the full set of fusion reactions. Purely analytical treatment of fuel cycle dynamic can very quickly become overwhelming, thus the dynamic fuel cycle modelling tool MINERVA is presented, built with the Julia ModelingToolkit language. It utilizes an acasual block-based approach to enable full species tracking and flexible architecture assessments.

A simplified direct internal recycling loop model comprehending a 0D plasma block is simulated in MINERVA using EU DEMO data. Depending on the protium production rate/source, protium accumulation poses a fundamental challenge at high DIR efficiencies in the absence of dedicated protium removal systems. Also, if no active fuel rebalancing measure is employed, D–T isotopic imbalances at the exhaust of the machine are amplified by the recycling of exhaust Q in the DIR. With that being said, the benefits of the DIR concept for fuel cycle efficiency are verified, with effective conversion ratios f_{eff} growing exponentially with DIR separation efficiency η_{DSS}.

An IFC architecture with a bypass loop within the DIR loop is proposed and applied to two case studies, the EU DEMO and GIGA reactors. The architecture successfully addresses the key challenges identified. The protium removal system effectively limits hydrogen accumulation well below 1.0% even at very high DIR efficiencies, enabling operation across the full practical range of separation factors. Isotope rebalancing via active control of D–T ratios through the storage system maintains optimal 50/50 fuel composition at the pellet injection location, requiring approximately between 1.29 (EU DEMO) and 1.35 (GIGA) deuterium-to-tritium ratio from storage due to isotopic effects in the protium removal system. The bypass loop provides an efficient mechanism for supplying density control gas, maintaining acceptable impurity levels. Significant reductions in external fuel requirements are achievable through bypass loop implementation.

Since this work primarily focuses on dilution at a system-level, it is yet to be seen if limitations might arise for specific phenomena within the reactor chamber, like the recycling of species in the divertor region. Further and more detailed analysis is this direction are needed. Moreover, this architecture, although generic, was optimized for EU DEMO. Further optimizations for stellarators may be possible to take design differences into account.

The present study lays the groundwork for more integrated fuel cycle modelling. Future work will focus on better plasma modelling, FC integration and chemical process modules. The addition of other physical processes within the reactor chamber will improve the fidelity of the 0D plasma model. The IFC model will be expanded to include the OUTL and OFC, thereby enabling actual closed-loop simulations of the full tritium cycle from plasma to storage and back. This integration will support more accurate estimations of tritium throughput, inventory and requirements. With the addition of the OUTL and OFC, models of specific chemical processing technologies will be essential to simulate the system. These enhancements will enable a more complete framework for future fusion fuel cycle design, supporting system optimization.

Symbols

$\langle \sigma v \rangle$ ($\mathrm{cm^3\,s^{-1}}$) Reaction rate
σ ($\mathrm{m^2\,s^{-1}}$) Cross-section
ν ($\mathrm{m\,s^{-1}nu}$) Velocity
T (keV) Temperature
n_e ($\mathrm{m^{-3}}$) Electron density
n_i ($\mathrm{m^{-3}}$) Density of species i
ρ (−) Normalized minor radius
R (m) Major radius
a (m) Minor radius
W_{fus} (GW) Fusion power
τ_E (s) Energy confinement time
τ_α^* (s) Effective α confinement time
τ_p (s) Particle (DT) confinement time
V_i ($\mathrm{m^3}$) Volume of component i
B_T (T) Total magnetic field
β (−) Beta
S_{FW} ($\mathrm{m^2}$) First wall surface
Γ ($\mathrm{s^{-1}}$) Particle flow rate
$k_{S_{FW}}$ (−) Effective outgassing FW surface multiplier
ξ^{max} (−) Maximum allowable concentration of impurities
P_{DT} (MPa) Fuel pressure
P_{tot}^{max} (MPa) Maximum total plasma pressure
E_f (MeV) Fusion energy per α particle
μ ($\mathrm{H\,m^{-1}}$) Magnetic permeability
f_i (−) Relative density of species i
f_{tot} (−) Total relative density
R_{rad} ($\mathrm{keV\,m^3\,s^{-1}}$) Radiation loss rate
L_i ($\mathrm{keV\,m^3\,s^{-1}}$) Cooling rate for species i
ρ^* (−) τ_α^*/tau_E
$\langle Z_i \rangle$ (−) Average charge of species i
N_i (−) Number of particles of species i
x_i (−) Atomic fraction for species i
S_i ($\mathrm{s^{-1}}$) Sink/source for species i
w_c (−) Reaction rate correction factor
RR ($\mathrm{m^6\,s^{-1}}$) Integral reaction rate
br (−) Branching ratio
η_f (−) Fuelling efficiency
f_b (−) Burning rate
$\bar{f}$ (−) Conversion factor
f_{eff} (−) Effective conversion factor
f_d (−) Dilution factor
τ_i (s) Residence time of system i
RS (−) Relative sensitivity index coefficient
RS^{norm} (−) Normalized relative sensitivity index
η_{DSS} (−) DIR Q separation fraction
η_{S1} (−) S1 separation fraction
η_{S2} (−) S2 separation fraction
η_{PR} (−) PR H separation efficiency

Acronyms

AZ Active Zone

CSTR Continuous-Stirred Tank Reactor

DIR Direct Internal Recycling

DSS DIR Q Separation System

EPS Exhaust Processing System

FC Fuel Cycle

FOM Figure Of Merit

FW First Wall

GDCM Gas Distribution Control and Monitoring

IFC Inner FUle Cycle

MINERVA Modelling and integration of Nuclear fusion Energy Reactor fuel cycle for Versatile Analysis

OAT One-At-a-Time

ODE Ordinary Differential Equation

OFC Outer FUle Cycle

PC Pressure Controller

PI Pellet Injection

PR Protium Removal

RC Reactor Chamber

RTM Residence Time Method

SOL Scrape-Off Layer

TSA Temperature Swing Adsorption

CRediT authorship contribution statement

Federico Hattab: Writing – review & editing, Writing – original draft, Visualization, Software, Methodology, Investigation, Formal analysis, Data curation, Conceptualization. **Yuri Igitkhanov:** Writing – review & editing, Supervision, Methodology, Investigation, Formal analysis, Conceptualization. **Vincenzo Narcisi:** Writing – review & editing, Supervision, Investigation. **Alessia Santucci:** Writing – review & editing, Supervision, Project administration. **Fabio Giannetti:** Writing – review & editing, Supervision, Funding acquisition. **Giulia Valeria Centomani:** Writing – review & editing, Funding acquisition. **Paul A. Staniec:** Writing – review & editing, Data curation. **Richard Kembleton:** Writing – review & editing. **Thomas Giegerich:** Writing – review & editing, Supervision, Project administration, Conceptualization.

Declaration of competing interest

The authors declare that they have no known competing financial interests or personal relationships that could have appeared to influence the work reported in this paper.

Acknowledgements

Project ECS 0000024 Rome Technopole, - CUP B83C22002820006, NRP Mission 4 Component 2 Investment 1.5, Funded by the European Union - NextGenerationEU.

This work has been carried out within the framework of the EUROfusion Consortium, funded by the European Union via the Euratom Research and Training Programme (Grant Agreement No 101052200 — EUROfusion). Views and opinions expressed are however those of the author(s) only and do not necessarily reflect those of the European Union or the European Commission. Neither the European Union nor the European Commission can be held responsible for them.

Appendix A. Active zone calcuation

Inside the plasma, fusion reactions (and thus the production of protium from them) happen in the region where a stable burn of tritium and production of energy takes place, i.e. where fusion reactions overcome losses. This region is called Active Zone, AZ, and outside it the temperature drops below the ignition point. The AZ can be roughly estimated from its definition, equating the reference reactor power and the integral over the AZ of the product between the DT reaction rate and the energy released per fusion reaction E_f (Eq. (A.1))

$$W_{fus} = E_f \pi^2 R k a^2 \int_0^{x_{az}} n(u)^2 \, \langle \sigma v \rangle_{DT}(u) \, u \, du \tag{A.1}$$

The normalized abscissa corresponding to the boundary of the AZ, x_{AZ}, is obtained by finding the root of Eq. (A.1). The calculation of the AZ is used in Appendix C to estimate the H production rate and in Section 4 in the lumped plasma model.

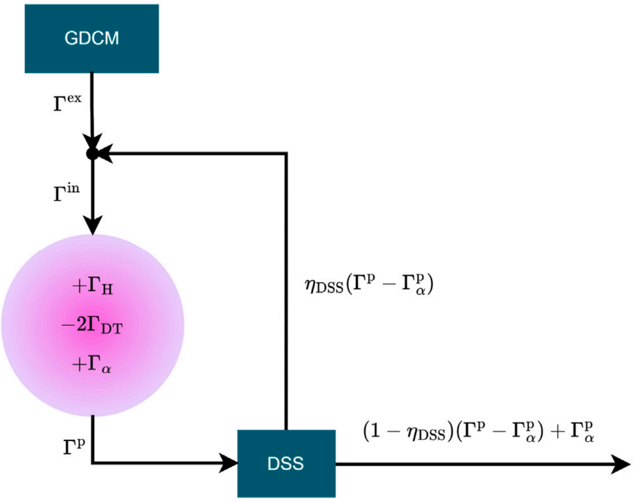

Fig. 21. Simplified scheme of direct internal recycling loop.

Appendix B. DIR extended analytical treatment

The most basic representation of the DIR loop is shown in Fig. 21. The DIR DSS separates a fraction η_{DSS} of the Q in the incoming exhaust from the stream. The separated Q is recirculated back to the fuelling system, mixing it with the flow coming from the Gas Distribution Control and Monitoring (GDCM) system before entering again the reactor chamber. Γ [s^{-1}] are particle flow rates, the superscripts p and in indicate the flow pumped out of the machine and the one incoming into the machine, respectively. Γ_H is the protium production rate from reactions Eqs. (1), (4), (6) and (8), and Γ_{DT} is the sink of D and T due to DT reactions. Γ_α, representing the helium production rate from DT reactions, is equal to Γ_{DT}. It is explicitly named for clarity and will be used interchangeably with Γ_{DT} hereinafter.

Starting from mass balances, it is possible to derive the time evolution of H inventory N_H in the RC. The final formula is Eq. (B.1), where $N_H(0)$ is the initial inventory and A* is a coefficient that will be derived in this section. Using Eq. (B.1), the trend for the protium inventory exhibits an asymptote for $t \to \infty$. The steady state value depends on Γ_H, and when it is larger than the sink (i.e. the quantity leaving the DIR through the DSS) an indefinite growth of N_H takes place.

$$N_H(t) = N_0 e^{-A^* t} + \frac{\Gamma_H}{A^*}(1 - e^{-A^* t}) \tag{B.1}$$

By writing a balance equation for each species involved in the fusion reactions Eqs. (1)–(8), (B.2)–(B.5) are obtained.

$$\Gamma^p_H = \Gamma^{in}_H + \Gamma_{DD1} + \Gamma_{\mathrm{DHe}^3} + \Gamma_{T\mathrm{He}^3(1+3)} \tag{B.2}$$

$$\Gamma^p_D = \Gamma^{in}_D - \Gamma_{DT} - 2\Gamma_{DD(1+2)} - \Gamma_{\mathrm{DHe}^3} + \Gamma_{T\mathrm{He}^3(2)} \tag{B.3}$$

$$\Gamma^p_T = \Gamma^{in}_T - \Gamma_{DT} + \Gamma_{DD(1)} - 2\Gamma_{TT} - \Gamma_{T\mathrm{He}^3(1+2+3)} \tag{B.4}$$

$$\Gamma^p_{\mathrm{He}} = \Gamma^{in}_{\mathrm{He}} + \Gamma_{DT} + \Gamma_{DD(2)} + \Gamma_{TT} \tag{B.5}$$

Summing the individual balance equations, the overall balance Eq. (B.6) is obtained.

$$\Gamma^p = \Gamma^{in} - \Gamma_{DT} + \Gamma_H - \Gamma_{misc} \tag{B.6}$$

where $\Gamma^{p/in} = \Gamma^{p/in}_H + \Gamma^{p/in}_D + \Gamma^{p/in}_T + \Gamma^{p/in}_{\mathrm{He}}$ and Γ_H and Γ_{misc} are defined according to Eqs. (B.7) and (B.8), respectively.

$$\Gamma_H = \Gamma_{DD(1)} + \Gamma_{\mathrm{DHe}^3} + \Gamma_{T\mathrm{He}^3(1+3)} \tag{B.7}$$

$$\Gamma_{misc} = \Gamma_{DD(1+2)} + \Gamma_{\mathrm{DHe}^3} + \Gamma_{T\mathrm{He}^3(1+3)} + \Gamma_{TT} \tag{B.8}$$

Γ_{DT} and Γ^{in} can be related to each other using the definition of burning fraction (Eq. (27)). Furthermore, the flow rate entering the RC Γ^{in} can be written as the sum of what is coming from outside the DIR loop, Γ^{ex} (e.g., from the GDCM), and what is being recirculated by the DSS, as described by Eq. (B.9).

$$\Gamma^{in} = \Gamma^{ex} + \eta_{DSS}\Gamma^{p} x_{Q}^{p} \tag{B.9}$$

x_Q^p is the atomic fraction of Q in the exhaust stream. Remembering the definition of $\bar{f}$ and defining a parameter $\mu^* = \eta_{DSS} x_Q^p (1 - \bar{f} x_T^{in})$, it is possible to combine Eqs. (27), (B.6) and (B.9) into an expression for the pumped flow rate that takes into account all the main parameters of the system (Eq. (B.10))

$$\Gamma_p = \frac{\Gamma^{ex}(1 - \bar{f} x_T^{in}) + \Gamma_H - \Gamma_{misc}}{1 - \mu^*} \tag{B.10}$$

Starting from Eq. (B.10), the associated protium streams leaving and entering the chamber can be expressed as $\Gamma_H^p = x_H^p \Gamma^p$ and $\Gamma_H^{in} = \eta_{DSS} x_H^p \Gamma^p$, respectively. x_H^p is the protium atomic concentration at the exhaust, that is further expressed as the ratio of the protium inventory N_H to the total inventory N_{tot} (assuming that it is the same as in the main plasma). By using these expressions, an ordinary differential equation for the time evolution of N_H in the RC is obtained (Eqs. (B.11) and (B.12)).

$$\frac{\partial N_H}{\partial t} = \Gamma_H + \Gamma_H^{in} - \Gamma_H^p = \Gamma_H - N_H A^* \tag{B.11}$$

$$A^* = \frac{1 - \eta_{DSS}}{N_{tot}} \frac{\Gamma^{ex}(1 - \bar{f} x_T^{in}) + \Gamma_H - \Gamma_{misc}}{1 - \mu^*} \tag{B.12}$$

The solution to the ODE Eq. (B.11) is known a it is Eq. (B.1). Although the problem is of simple analytical derivation, the solution is not straightforward without doing simplifying assumptions, due to its nonlinear nature.

Appendix C. Protium production rate from fusion reactions

Once the AZ is known, the protium production rate can be computed from integrating the reaction rates of the reactions that yield protium over the AZ volume (Eqs. (C.1) to (C.3)). Eq. (C.1) gives the protium production rate as the sum of the protium production contributions from $\mathrm{D-D}$ (50%), $\mathrm{D-He^3}$ and $\mathrm{T-He^3}$ (51+6%) reactions. Eq. (C.2) give the particle production rate Γ [s − 1] from the generic reaction between species j and y as the integral of the reaction rate (Eq. (C.3)) over the active zone volume.

$$\Gamma_H = \left(\Gamma_{DD,50\%} + \Gamma_{\mathrm{DHe}^3} + \Gamma_{\mathrm{THe}^3,51+6\%}\right)/\mathrm{Na} \tag{C.1}$$

$$\Gamma_{jy} = b r_{jy} k a^2 R \pi^2 \int_0^{x_{AZ}} n(u)^2 \cdot \langle\sigma v\rangle_{jy}(u) \cdot u \, du \tag{C.2}$$

$$\langle\sigma v\rangle_{jy}(u) = A_{jy} T(u)^{-B_{jy}} \exp\left(-C_{jy} T(u)^{-D_{jy}}\right) \tag{C.3}$$

Using reference data for EU DEMO, a protium production rate of $5.37 \times 10^{18}\ \mathrm{s}^{-1}$ is found (red dot in Fig. 22), which is about 0.76% of the α particles production rate. This production rate is more sensible on variations of the temperature level than on the size of the active zone. This is shown in Fig. 22, where a two-dimensional analysis is done scanning AZ sizes and on axis temperatures. The temperature profile is scaled according to the $T0$ value, following the same profile shape. Given the parameter space investigated, the rate variation is limited to ∼±25%.

Data availability

Data will be made available on request.

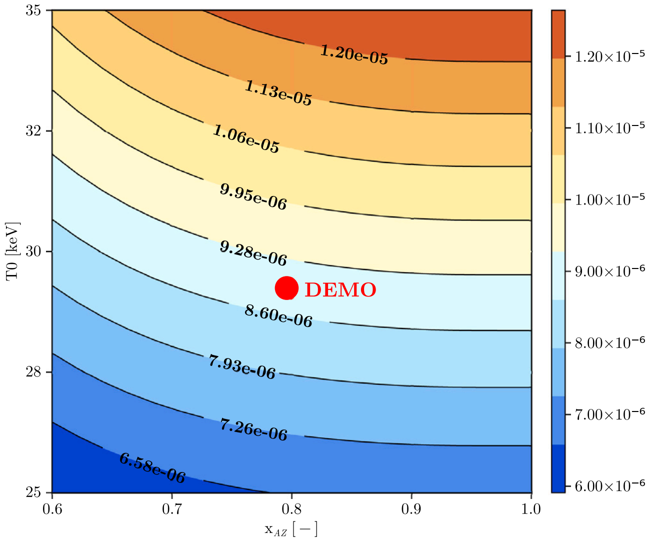

Fig. 22. Protium production rate as a function of on axis temperature $T0$ and active zone normalized radius x_{AZ}. The red dot is the value obtained with the EU DEMO 2018 design data.

References

[1] Chr. Day, B. Butler, T. Giegerich, B. Ploeckl, S. Varoutis, A smart three-loop fuel cycle architecture for DEMO, Fusion Eng. Des. 146 (2019) 2462–2468, SI:SOFT-30.

[2] Chr. Day, B. Butler, T. Giegerich, P.T. Lang, R. Lawless, B. Meszaros, Consequences of the technology survey and gap analysis on the EU demo R&D programme in tritium, matter injection and vacuum, Fusion Eng. Des. 109–111 (2016) 299–308, Proceedings of the 12th International Symposium on Fusion Nuclear Technology-12 (ISFNT-12).

[3] Chr. Day, K. Battes, B. Butler, S. Davies, L. Farina, A. Frattolillo, R. George, T. Giegerich, S. Hanke, T. Härtl, Y. Igitkhanov, T. Jackson, N. Jayasekera, Y. Kathage, P.T. Lang, R. Lawless, X. Luo, C. Neugebauer, B. Ploeckl, A. Santucci, J. Schwenzer, T. Teichmann, T. Tijssen, S. Tosti, S. Varoutis, A. Vazquez Cortes, The pre-concept design of the DEMO tritium, matter injection and vacuum systems, Fusion Eng. Des. 179 (2022) 113139.

[4] A. Loarte, F. Liu, G.T.A. Huijsmans, A.S. Kukushkin, R.A. Pitts, MHD stability of the ITER pedestal and SOL plasma and its influence on the heat flux width, J. Nucl. Mater. 463 (2015) 401–405, PLASMA-SURFACE INTERACTIONS 21.

[5] F. Subba, D.P. Coster, M. Moscheni, M. Siccinio, SOLPS-ITER modeling of divertor scenarios for EU-DEMO, Nucl. Fusion 61 (10) (2021) 106013.

[6] Mohamed Abdou, Marco Riva, Alice Ying, Christian Day, Alberto Loarte, LR Baylor, Paul Humrickhouse, Thomas F Fuerst, Seungyon Cho, Physics and technology considerations for the deuterium–tritium fuel cycle and conditions for tritium fuel self sufficiency, Nucl. Fusion 61 (1) (2020) 013001.

[7] M. Coleman, Y. Hörstensmeyer, F. Cismondi, DEMO tritium fuel cycle: performance, parameter explorations, and design space constraints, Fusion Eng. Des. 141 (2019) 79–90.

[8] Samuele Meschini, Sara E. Ferry, Rémi Delaporte-Mathurin, Dennis G. Whyte, Modeling and analysis of the tritium fuel cycle for ARC- and STEP-class D-T fusion power plants, Nucl. Fusion 63 (12) (2023) 126005.

[9] Yingbo Ma, Shashi Gowda, Ranjan Anantharaman, Chris Laughman, Viral Shah, Chris Rackauckas, ModelingToolkit: A composable graph transformation system for equation-based modeling, 2021.

[10] Christopher Rackauckas, Qing Nie, Differentialequations.jl–a performant and feature-rich ecosystem for solving differential equations in julia, J. Open Res. Softw. 5 (1) (2017) 15.

[11] Joseph Donald Huba, NRL Plasma Formulary, Vol. 6790, Naval Research Laboratory, 1998, 98–358.

[12] M. Siccinio, W. Biel, M. Cavedon, E. Fable, G. Federici, F. Janky, H. Lux, F. Maviglia, J. Morris, F. Palermo, O. Sauter, F. Subba, H. Zohm, DEMO physics challenges beyond ITER, Fusion Eng. Des. 156 (2020) 111603.

[13] M. Siccinio, J.P. Graves, R. Kembleton, H. Lux, F. Maviglia, A.W. Morris, J. Morris, H. Zohm, Development of the plasma scenario for EU-DEMO: Status and plans, Fusion Eng. Des. 176 (2022) 113047.

[14] E.J. Strait, Stability of high beta tokamak plasmas*, Phys. Plasmas 1 (5) (1994) 1415–1431.

[15] John Wesson, David J. Campbell, Tokamaks, Vol. 149, Oxford University Press, 2011.

[16] D. Reiter, G.H. Wolf, H. Kever, Burn condition, helium particle confinement and exhaust efficiency*, Nucl. Fusion 30 (10) (1990) 2141.

[17] A. A. Mavrin and, Improved fits of coronal radiative cooling rates for high-temperature plasmas, Radiat. Eff. Defects Solids 173 (5–6) (2018) 388–398.

[18] T. Pütterich, E. Fable, R. Dux, M. O'Mullane, R. Neu, M. Siccinio, Determination of the tolerable impurity concentrations in a fusion reactor using a consistent set of cooling factors, Nucl. Fusion 59 (5) (2019) 056013.

[19] Aleksey A. Mavrin, Effect of impurity radiation and helium particle confinement on tokamak–reactor plasma performance, Plasma Phys. Control. Fusion 62 (10) (2020) 105023.

[20] William Kuan, Mohamed A. Abdou and, A new approach for assessing the required tritium breeding ratio and startup inventory in future fusion reactors, Fusion Technol. 35 (3) (1999) 309–353.

[21] B.J. Peters, S. Hanke, C. Day, Metal foil pump performance aspects in view of the implementation of direct internal recycling for future fusion fuel cycles, Fusion Eng. Des. 136 (2018) 1467–1471, Special Issue: Proceedings of the 13th International Symposium on Fusion Nuclear Technology (ISFNT-13).

[22] Yuichi Ishikawa, Vincenc Nemanič, An overview of methods to suppress hydrogen outgassing rate from austenitic stainless steel with reference to UHV and EXV, Vacuum 69 (4) (2003) 501–512.

[23] M. Bernardini, S. Braccini, R. De Salvo, A. Di Virgilio, A. Gaddi, A. Gennai, G. Genuini, A. Giazotto, G. Losurdo, H.B. Pan, A. Pasqualetti, D. Passuello, P. Popolizio, F. Raffaelli, G. Torelli, Z. Zhang, C. Bradaschia, R. Del Fabbro, I. Ferrante, F. Fidecaro, P. La Penna, S. Mancini, R. Poggiani, P. Narducci, A. Solina, R. Valentini, Air bake-out to reduce hydrogen outgassing from stainless steel, J. Vac. Sci. Technol. A 16 (1) (1998) 188–193.

[24] P. Marin, M. Dialinas, G. Lissillour, A. Marraud, A. Reboux, Outgassing performances of an industrial prototype tube for the virgo antenna, Vacuum 49 (4) (1998) 309–314.

[25] G. Messer, N. Treitz, Sensitive mass-selective outgassing rate measurements on baked stainless steel and cu samples, in: Proceedings of the Seventh International Vacuum Congress and the Third International Conference on Solid Surfaces, Vol. 1, 1977.

[26] Vincenc Nemanic, Janez Setina, Outgassing in thin wall stainless steel cells, J. Vac. Sci. Technol. A 17 (3) (1999) 1040–1046.

[27] Vincenc Nemanic, Janez Setina, Experiments with a thin-walled stainless-steel vacuum chamber, J. Vac. Sci. Technol. A 18 (4) (2000) 1789–1793.

[28] Cyra Neugebauer, Y. Hörstensmeyer, C. Day and, Technology development for isotope rebalancing and protium removal in the EU-DEMO fuel cycle, Fusion Sci. Technol. 76 (3) (2020) 215–220.

[29] L.R. Baylor, T.C. Jernigan, P.B. Parks, G. Antar, N.H. Brooks, S.K. Combs, D.T. Fehling, C.R. Foust, W.A. Houlberg, G.L. Schmidt, Comparison of deuterium pellet injection from different locations on the DIII-D tokamak, Nucl. Fusion 47 (11) (2007) 1598.

[30] Christian Day, Thomas Giegerich, The direct internal recycling concept to simplify the fuel cycle of a fusion power plant, Fusion Eng. Des. 88 (6) (2013) 616–620, Proceedings of the 27th Symposium On Fusion Technology (SOFT-27); Liège, Belgium, September 24-28, 2012.

[31] Tim Teichmann, Xueli Luo, Thomas Giegerich, Christian Day and, Study of the effective torus exhaust high vacuum pumping system performance in the inner tritium plant loop of EU-DEMO, Fusion Sci. Technol. 80 (3–4) (2024) 399–410.